Project Report
STK-221
Volume II

Proceedings of the 1994 Space Surveillance Workshop

K.P. Schwan
Editor

5–7 April 1994

Lincoln Laboratory
MASSACHUSETTS INSTITUTE OF TECHNOLOGY
LEXINGTON, MASSACHUSETTS

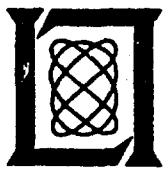

Prepared with partial support of the Department of the Air Force
under Contract F19628-90-C-0002.

Prepared with partial support of the Department of the Air Force under Contract F19628-90-C-0002.

The ESC Public Affairs Office has reviewed this report, and it is releasable to the National Technical Information Service, where it will be available to the general public, including foreign nationals.

This technical report has been reviewed and is approved for publication.

FOR THE COMMANDER

Gary Tutungian
Administrative Contracting Officer
Directorate of Contracted Support Management

MASSACHUSETTS INSTITUTE OF TECHNOLOGY
LINCOLN LABORATORY

PROCEEDINGS OF THE 1994 SPACE SURVEILLANCE WORKSHOP

PROJECT REPORT STK-221
VOLUME II

5–7 APRIL 1994

The twelfth Annual Space Surveillance Workshop held on 5–7 April 1994 was hosted by MIT Lincoln Laboratory and provided a forum for space surveillance issues. This *Proceedings* documents most of the presentations, with minor changes where necessary.

LEXINGTON MASSACHUSETTS

TABLE OF CONTENTS

PREFACE

The Twelfth Annual Space Surveillance Workshop sponsored by ESC and hosted by MIT Lincoln Laboratory was held on 5, 6 and 7 April 1994. The purpose of this series of workshops is to provide a forum for the presentation and discussion of space surveillance issues.

This *Proceedings* (Volume II) contains unclassified presentations from this workshop received after the deadline for Volume I. The papers were reproduced directly from copies supplied by their authors (with minor mechanical changes where necessary). It is hoped that this publication will enhance the utility of the workshop.

Kurt P. Schwan
Editor

The Quest for Russian Optical Surveillance Technology

Briefing Presented to the

12th Space Surveillance Workshop

MIT Lincoln Laboratory

by

Lt Col John Rabins

Commander, 1st Command & Control Squadron

5 April 1994

Overview

- Introduction
- Background
- Russian Institutes Visited
- Team Observations
- A Quick Tour of Russia

Introduction

The 1st Command & Control Squadron:

- Maintains accurate positional data on all earth orbiting satellites and debris
- Provides command & control for 26 worldwide space surveillance sensors
- Provides spacetrack data and products to various users

Data Flow

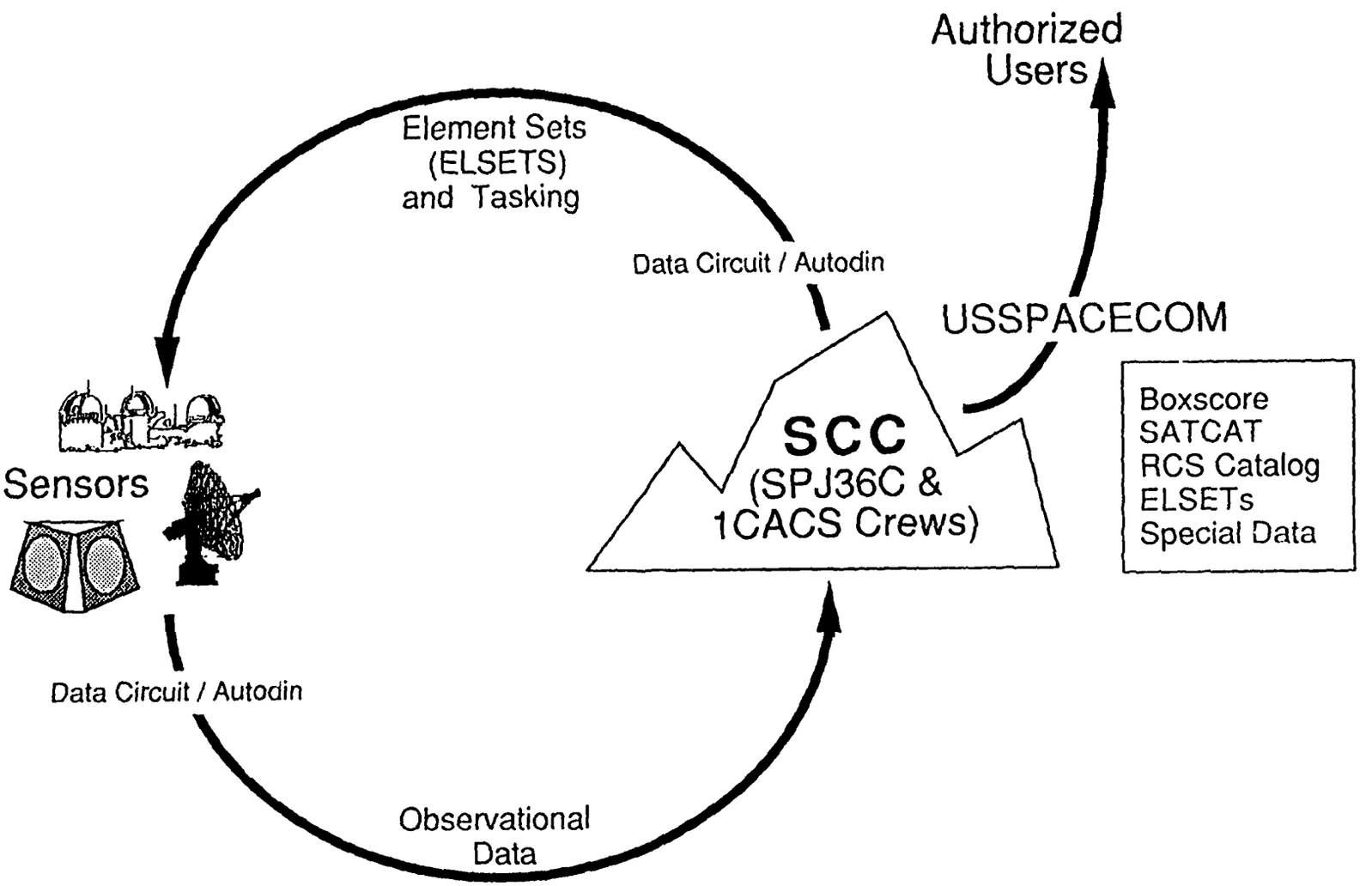
Authorized Users
Element Sets (ELSETS) and Tasking
Data Circuit / Autodin
USSPACECOM
Boxscore
SATCAT
RCS Catalog
ELSETs
Special Data
SCC
(SPJ36C & 1CACS Crews)
Sensors
Data Circuit / Autodin
Observational Data

Background

International Space Technology Assessment Program (ISTAP)

- **Purpose** - - Take advantage of unique Russian space technology and hardware following breakup of former Soviet Union

- **Multi-agency**
  - •• Air Force Space Command
  - •• Air Force Materiel Command
  - •• BDI, Inc.
  - •• DOE
  - •• Phillips Laboratory

- **Technology of interest** - - Optical Phase Conjugation (OPC)

Illustration of the Aberration-Correction Properties of Phase Conjugation

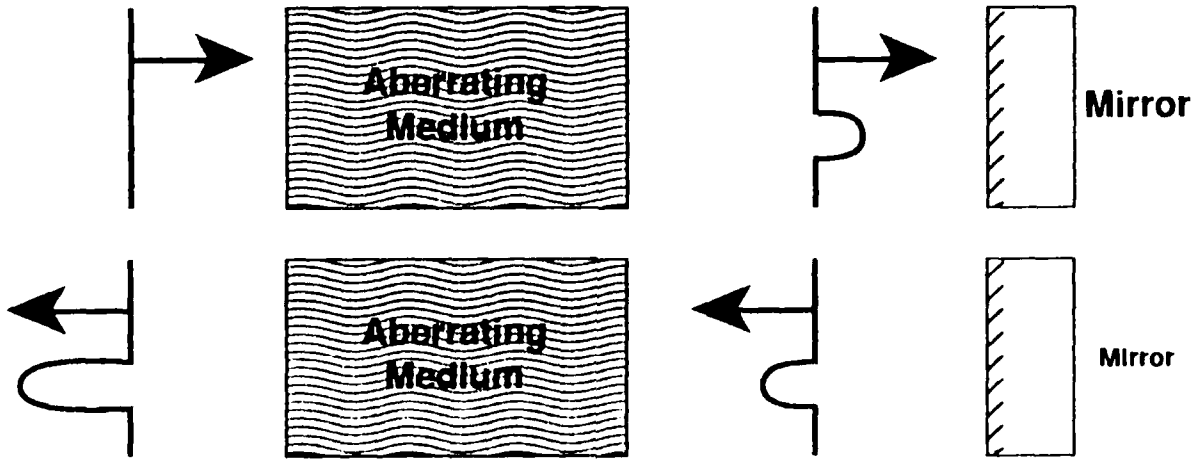

A standard mirror retains the sign of the phase error and the error is doubled

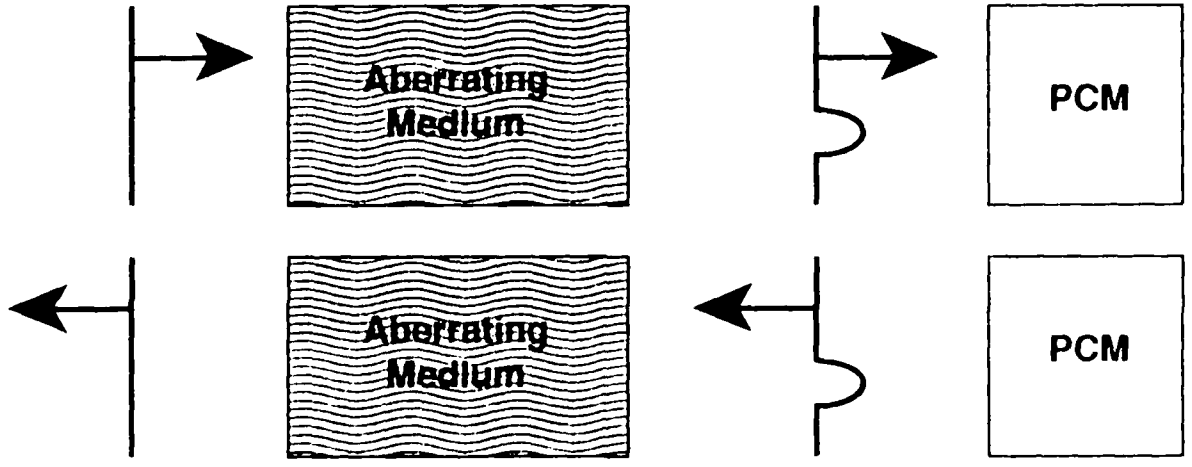

A phase conjugate mirror (PCM) reverses the sign of the phase error and the error cancels

Comparison of a Conventional Mirror Reflection and a Phase-Conjugate Mirror Reflection

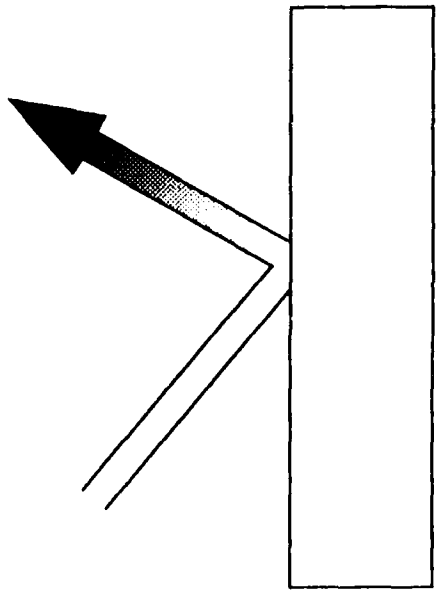

Conventional Mirror

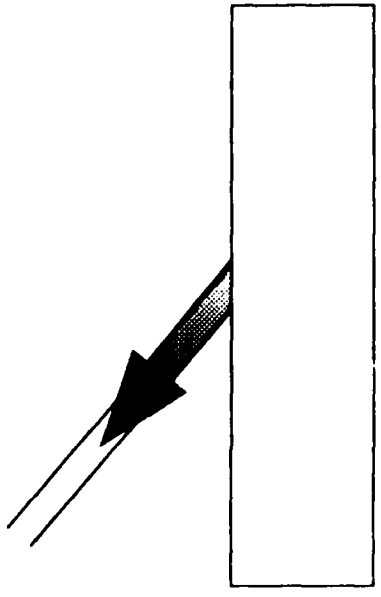

Phase-Conjugate Mirror

Optical Phase Conjugation by Four-Wave Mixing

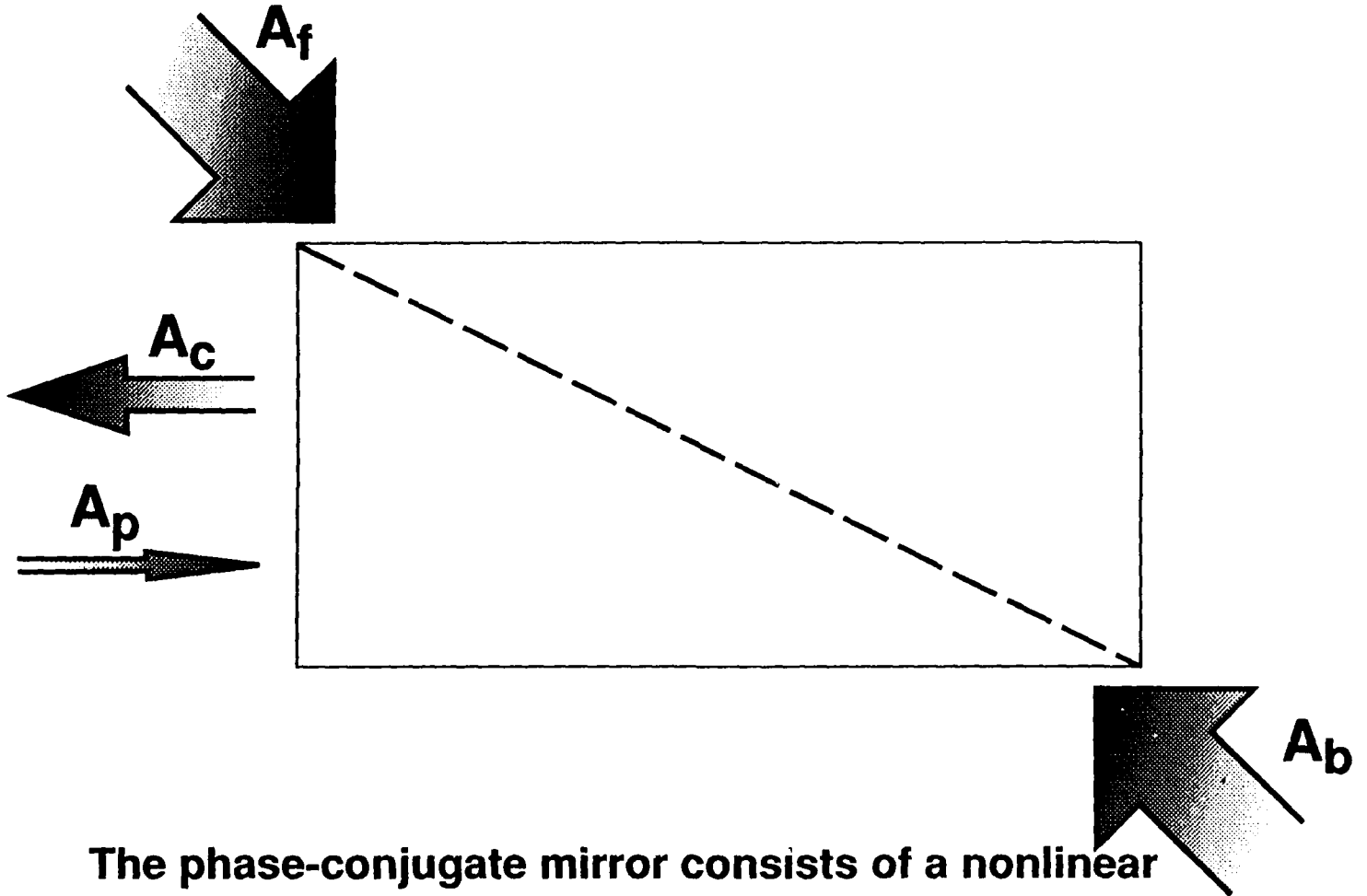

The phase-conjugate mirror consists of a nonlinear medium interacting with two counterpropagating pump beams A_f and A_b. The signal beam A_p emerges amplified and conjugate as A_c.

High Gain Configuration of Phase Conjugate Mirror (PCM)

The Gain Medium is Double Passed

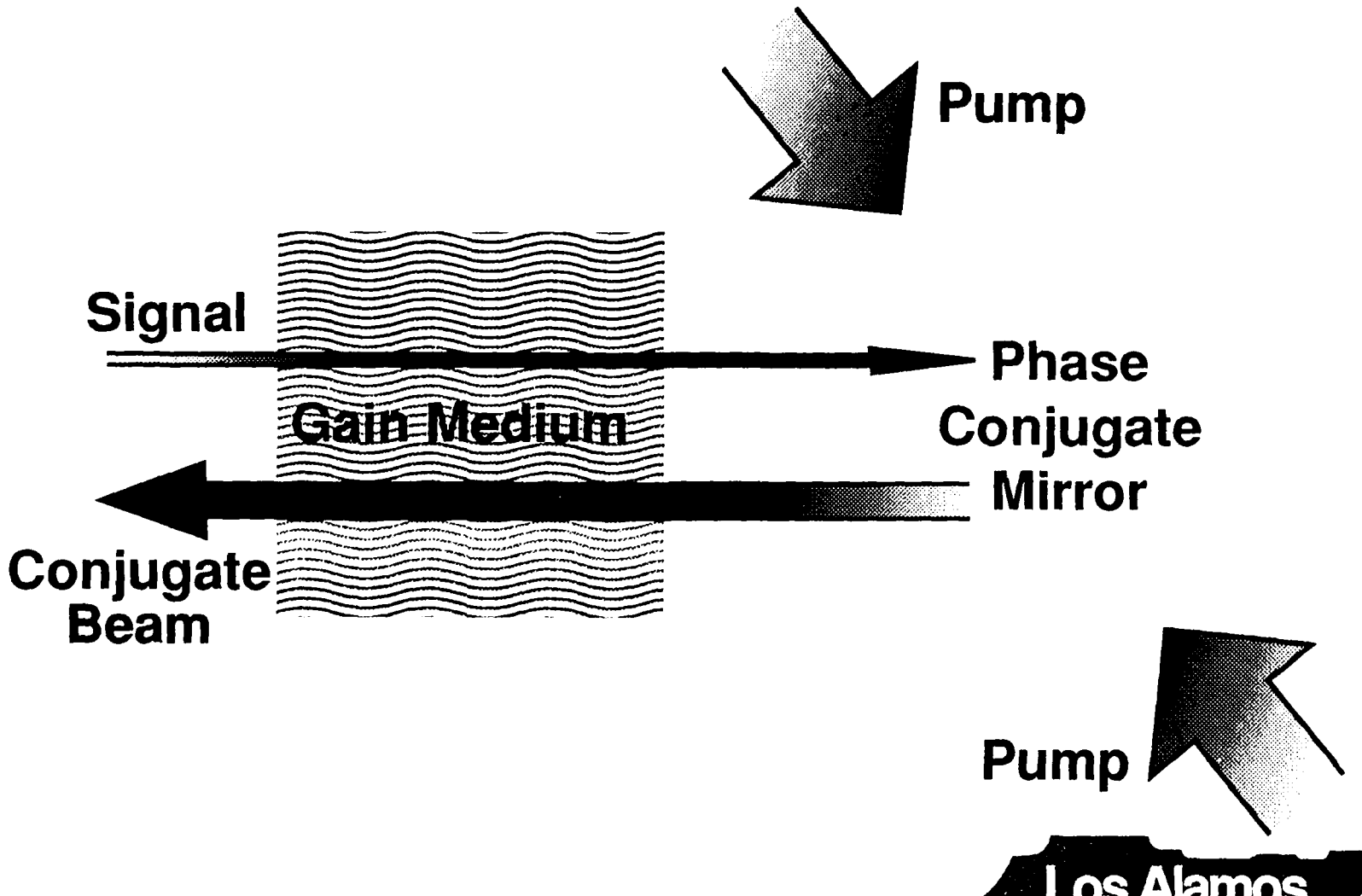

Potential Applications of OPC

- High power lasers
- Long baseline phased arrays for high resolution imaging
- Long baseline phased arrays for power beaming
  - Power sourcing
  - Boosting to higher orbit
- Analog image processing and image restoration
- Space debris tracking

Glint Returns to Target as High-Energy Beam

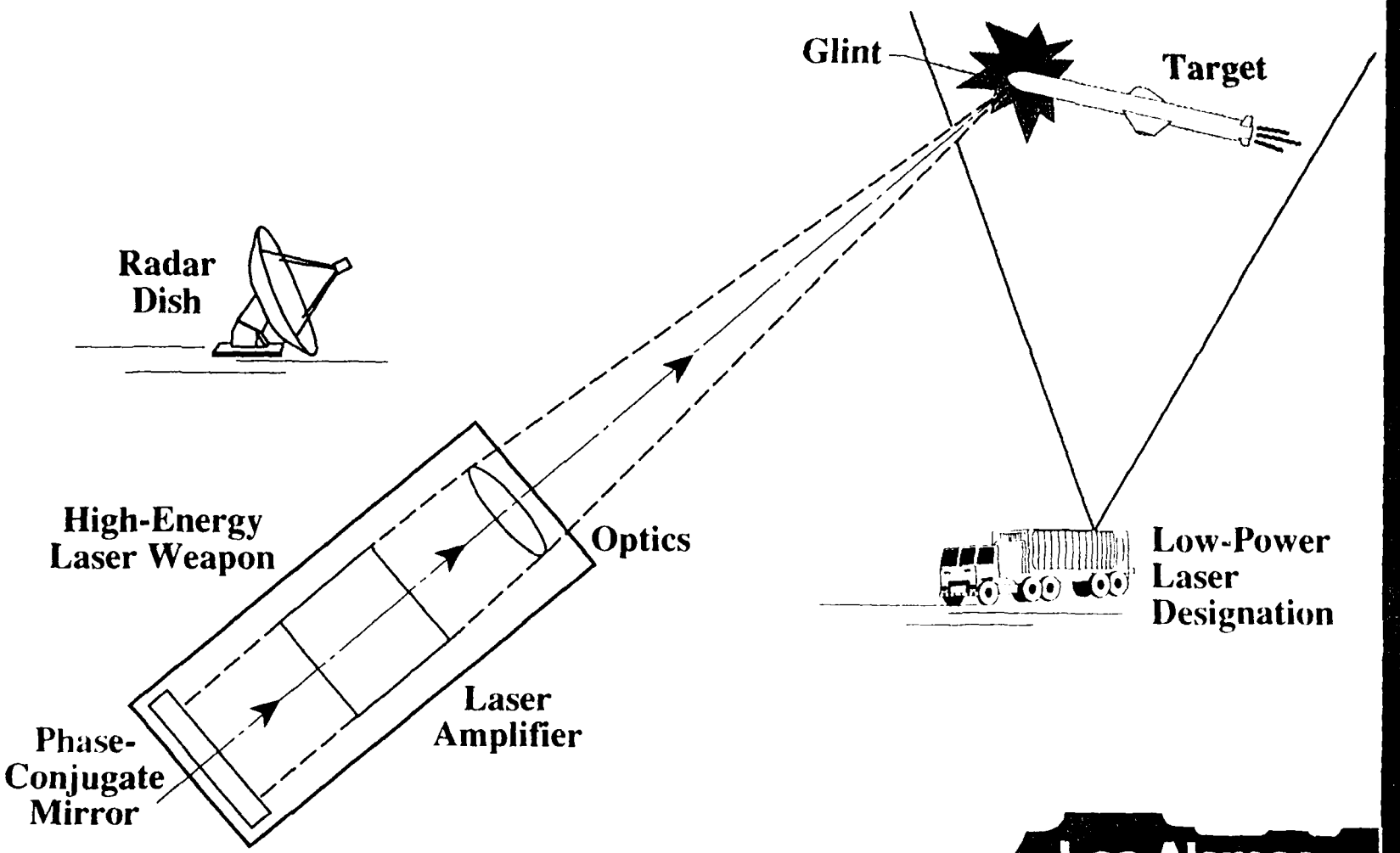

Space Catalog Snapshot (22Feb)

	Cataloged	Lost	1CACS Analyst Sats	Other Analyst Sats
NE	5676	43	459	163
DS	1342	79	603	115
Total	7018	122	1062	278

Total # of elsets in SATF = 8358

This does <u>not</u> reflect the total number of earth-orbiting objects!

Application of Interest: Spacetrack of Small Objects

- Purpose:
  - •• Provide NASA data on the debris environment below 10 cm for space station shielding design
  - •• Provide NASA operational collision avoidance data
- From SOW:

  1 cm diameter
  0.1 albedo (10% diffuse reflectivity)
  1000 km range
  7 km/sec
  1 km positional accuracy (1 sigma)
  0.25 m/sec orbital speed accuracy (1 sigma)

Russian Institutes Visited

State Owned

- Vavilov State Optical Institute (St. Petersburg)
- NPO Astrofizika (Moscow)
- Institute of Applied Physics (Nizhny-Novgorod)
- Radio Physical Institute (Nizhny-Novgorod)
- Kometa (Moscow)
- Russian Institute of Space Device Engineering (Moscow)

Private Companies

- Passat (Nizhny-Novgorod)
- Laser Systems, Inc. (Moscow)

Team Observations (trip 1)

- They didn't show us everything
  - •• Tours were obviously sanitized
  - •• Lots of work still highly classified
- We are convinced they've done some very important work
  - •• Open discussion regarding KW class lasers in space and vaporization of debris
- We sensed a real willingness to show us more in time

Team Observations (trip 2)

- The Russian government demonstrated heightened sensitivity about our intended purpose for dual-use technology
  - •• NPO Astrofizika meeting cancelled at last minute
  - •• Behind the scenes tension between government and institutes
  - •• State Committee for Defense Industry concerns
- The possibility of limited collaboration in space surveillance operations appears high
  - •• Promising areas in satellite catalog maintenance
  - •• Invitations to visit optical facilities in Caucasus and Central Asia

A Quick Tour of Russia

"Whenever you are unhappy, go to Russia. Anyone who has come to understand that country will find himself content to live anywhere else."

- Marquis de Custine
Russia in 1839

General Observations

- - 30 degrees is <u>mild</u> weather

General Observations

- - 30 degrees is mild weather

- **Motel 6 is a 5-star hotel**
  - **But - - Russians are extremely hospitable**

General Observations

- - 30 degrees is mild weather

- Motel 6 is a 5-star hotel
  - But - - Russians are extremely hospitable

- **Russian architecture is striking**
  - **Texas has nothing on them**

Utility of the MSX UVISI Instrument to Space Surveillance: Imaging, Tracking and Identification

P. F. Bythrow, R. L. Waddell, Pat Murphy and J. F. Carbary

The Johns Hopkins University Applied Physics Laboratory, Laurel, MD 20723

ABSTRACT

The UVISI Instrument of the Midcourse Space Experiment (MSX) consists of four imagers and five spectrographic imagers (SPIMs) using intensified CCD detectors for imaging and determination of target spectral content. UVISI incorporates 1750A based Image and Track processors to conduct target selection, track file computations and trajectory determination. The UVISI Imagers use a filter wheel arrangement to cover the wavelength domain from 110 nm to 900 nm in selectable bands. Imager sensitivity is of the order of 5 photons/cm^2sec. Intrascene dynamic range is 4096, while an interscene dynamic range of ~10^5 is allowed by the micro channel plate (MCP). This broad dynamic range allows UVISI to view dim objects in deep space as well as near earth objects against a sunlit earth background. SPIMs cover the same wavelength regime as the imagers and have similar sensitivity. The SPIMs have spectral resolution of ~0.5 - 4.0 nm. This paper will describe these characteristics in greater detail and discuss how UVISI's unique capabilities can be applied to the space surveillance task. Specifically UVISI has the potential for discrimination, viewing and tracking Resident Space Objects (RSOs) against a sunlit earth and earth limb as well as deep space. UVISI also has the unique potential to conduct multispectral Space Object Identification (SOI) by the identification of specific reflectance spectra from various RSO component materials.

1. INTRODUCTION

The Midcourse Space Experiment (MSX) is a spacecraft mission sponsored by the Ballistic Missile Defense Organization. The mission's principal design objective is to gather data on targets and backgrounds, both deep-space and near-Earth. The spacecraft has been developed and integrated by the Johns Hopkins University Applied Physics Laboratory (APL), and is due to be launched in November 1994. Major sensor systems, developed by APL, Utah State University's Space Dynamics Laboratory and MIT's Lincoln Laboratory, include the UVISI ultraviolet and visible imagers and spectrographs (APL), the SPIRIT III infrared imager and interferometer (USU/SDL), and the SBV space-based visible sensor (MIT/LL). The spacecraft is designed for a five year lifetime after being launched into a near-sun-synchronous orbit of ~ 900 kilometers, inclined about 99.2 degrees. A sophisticated attitude control and determination system and a closed-loop tracking system are integral to the data collection experiments.

The UVISI instrument derives from a succession of ultraviolet and visible instruments flown on other APL orbital missions over the past decade for the Department of Defense and NASA. The AIM (Auroral Ionospheric Mapper) flew on the HILAT spacecraft in 1983[1], and its cousin the AIRS (Auroral Ionospheric Remote Sensor) flew on the Polar BEAR spacecraft in 1986[2]. Both instruments made measurements of the ultraviolet aurora against a sunlit Earth. The Hopkins Ultraviolet Telescope made astronomical measurements of 77 celestial objects from the Shuttle STS-35 mission in 1990[3]. APL instruments also flew on the Department of Defense/Strategic Defense Initiative series of Delta missions. These instruments made the first exoatmospheric observations of UV plume phenomena and the first multi-spectral observations of an RSO from orbit[4,5,6].

2. INSTRUMENT OVERVIEW

UVISI consists of a suite of five spectrographic imagers, four imagers, an image processor subsystem, and various other electronic control and data handling subsystems. Figure 1 shows the block diagram of the UVISI system and indicates the major subsystems of the instrument. Each sensor (SPIM or Imager) has an independent power supply (converter) and sensor electronics units (SEU) that allows it to operate autonomously should any of the other sensors fail. (The SPIMs are numbered 1 through 5 according to the spectral regime, with SPIM1 sampling the far ultraviolet and SPIM5 sampling the visible. The imagers are labeled according to spectral regime and field of view. Thus, IUN indicates imager, ultraviolet, narrow-field.) The data control system (DCS) accepts commands from the spacecraft and formats and sends digital data from the sensors back to the spacecraft and to the UVISI image processor. The DCS has a backup in case of failure of the primary subsystem. The image processor reduces the raw image data from any one of the four imagers and directs the results to the spacecraft tracking processor. The track processor may then use target data from the image processor to slew the spacecraft or the spacecraft may be pointed open loop and the track file accumulated and stored for later analysis.

Figure 2 shows the mounting locations of the UVISI sensors on the MSX satellite. The satellite is three-axis stabilized and has a ring laser gyro/star-camera attitude determination system. All UVISI sensors are mounted on the periphery of the main spacecraft truss assembly and share a common boresight direction. For target tracking and attitude control the entire spacecraft is slewed in azimuth elevation and roll by means of four momentum wheels. Excess momentum is dumped magnetically by means of 3-axis control rods. The spacecraft can be slewed in azimuth and elevation at up to 1.6°/sec with accelerations of up to 0.03°/sec^2. Post processed attitude can be determined to 1.8 arcsec while, on-board attitude can be determined to 0.1°. The on-board attitude is stabilized during a data collection event to 1.8 arcsec/sec.

The five spectrographic imagers (SPIMs) provide two-dimensional maps of the spectra of various objects and scenes. Although primary SPIM observations are the atmospheric dayglow and nightglow, aurora, stars, zodiacal light, and plume trails, it is

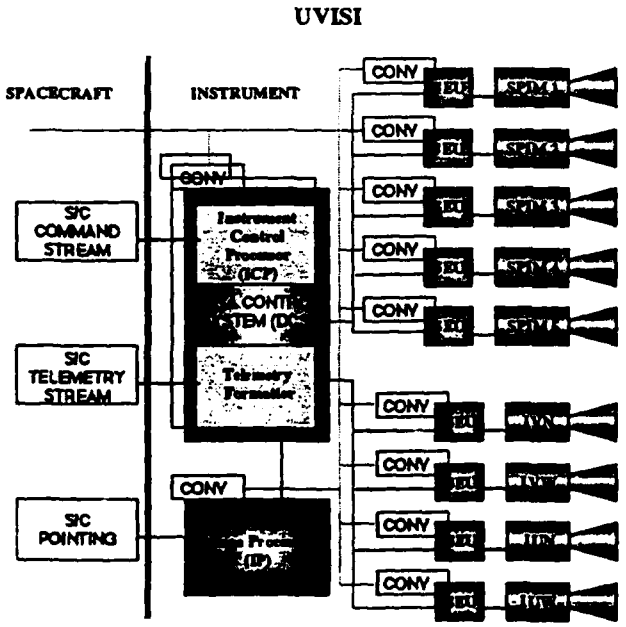

Fig. 1. Block diagram of UVISI showing the major subsystems and their interconnections.

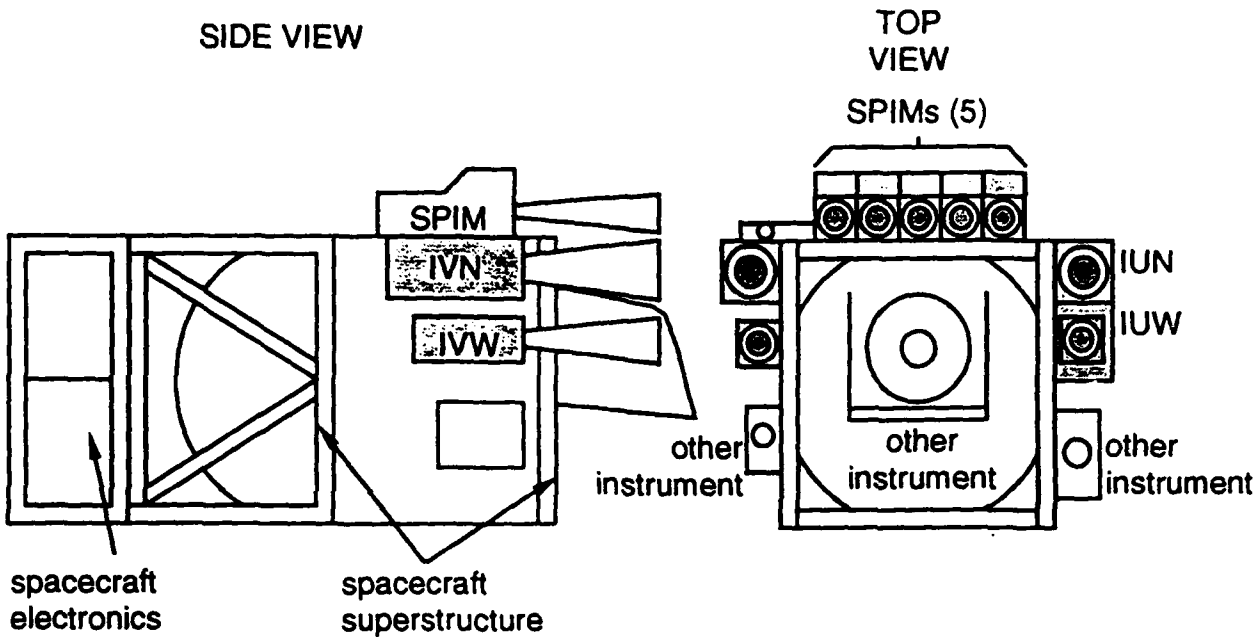

Fig. 2. Mounting locations of the UVISI sensors on the MSX spacecraft. All sensors have a common boresight.

possible to conduct spectrographic imaging of low altitude RSOs. When suitably inverted, SPIM radiance measurements will reveal atmospheric properties such as species concentrations, temperatures, and altitude profiles.[7,8,9] SPIM investigations of auroral radiance can provide estimates of the fluxes and energies of precipitating particles that cause auroral emissions [10]. SPIM observations will also measure the diffuse ultraviolet background of the sky [5]. Finally, SPIM observations have the potential to provide composition information on nearby RSOs.

The four imagers provide both wide-field and narrow-field images, in selectable wavelength bands, of the scenes that the SPIMs observe and will supply target tracking information for use by the image processor, track processor and satellite control system. The imagers provide information on the spatial content of the scene to a resolution of ~100 μrad or ~ 20 arcsec. Also, the imagers take one snapshot of the scene every 0.5 or 0.25 seconds, which provides a much higher time resolution than the SPIMs. Thus, the imagers can observe the time-evolution of the scene and target.

3. IMAGERS

The two UVISI narrow-field imagers share a common optical design, shown in the top diagram of Fig. 3. Each NFOV imager has a rectangular field of 1.6° x 1.3°, which translates to a pixel size of about 100 μrad in the 256x244 format of the CCD. One of the NFOV imagers has an RbTe photocathode that responds to photons in the middle ultraviolet (200-300 nm), which is the so-called "solar-blind" spectral regime. The other NFOV imager has an ExtS20 (bialkali) photocathode that responds to photons in the near ultraviolet and visible (300-800 nm). Both sensors use reflecting optics of a Cassegrainian design. Each NFOV imager has a 6-position filter wheel, one position of which is a closed or opaque filter. Each NFOV imager also has an effective collecting area of 130 cm^2.

The two UVISI wide-field imagers do not have a common design. Each WFOV imager has a rectangular field of 13.1° x 10.5°, which translates to a pixel size of about 800 μrad. To save weight and volume, the WFOV visible imager (Fig. 3, middle diagram) employs a 4-element refractive lens design. The WFOV ultraviolet imager (Fig. 3, bottom diagram) responds to far-ultraviolet photons (110-200 nm)

and must employ fully reflective optics. The WFOV ultraviolet imager uses three-element reflective optics. As with the NFOV imagers, each WFOV imager has a six-element filter wheel with one position opaque.

4. SPECTROGRAPHIC IMAGERS

Figure 4 shows a schematic diagram of a spectrographic imager. All UVISI SPIMs have a common, off-axis design that employs three-element reflecting optics. A scan mirror sweeps the field of view through 1.0° and sends light through a five-position filter/slit mechanism. A collimating mirror directs the light from the slit to a curved grating, which was mechanically-ruled. The spacing of the gratings differ for each SPIM in order to provide the desired dispersive characteristics. The grating itself serves to focus the dispersed light on a two-dimensional focal plane. One dimension of the focal plane represents a spatial dimension of 1°, while the other dimension represents a spectral dimension equal to the dispersion of the spectrograph. One complete 2D spatio-spectrogram results from each measurement at each mirror position. The five position slit/filter mechanism provides two slit sizes (1.0°x0.10° and 1.0°x0.05°) and various blocking-filters that eliminate extraneous spectral orders and long-wavelength contaminants.

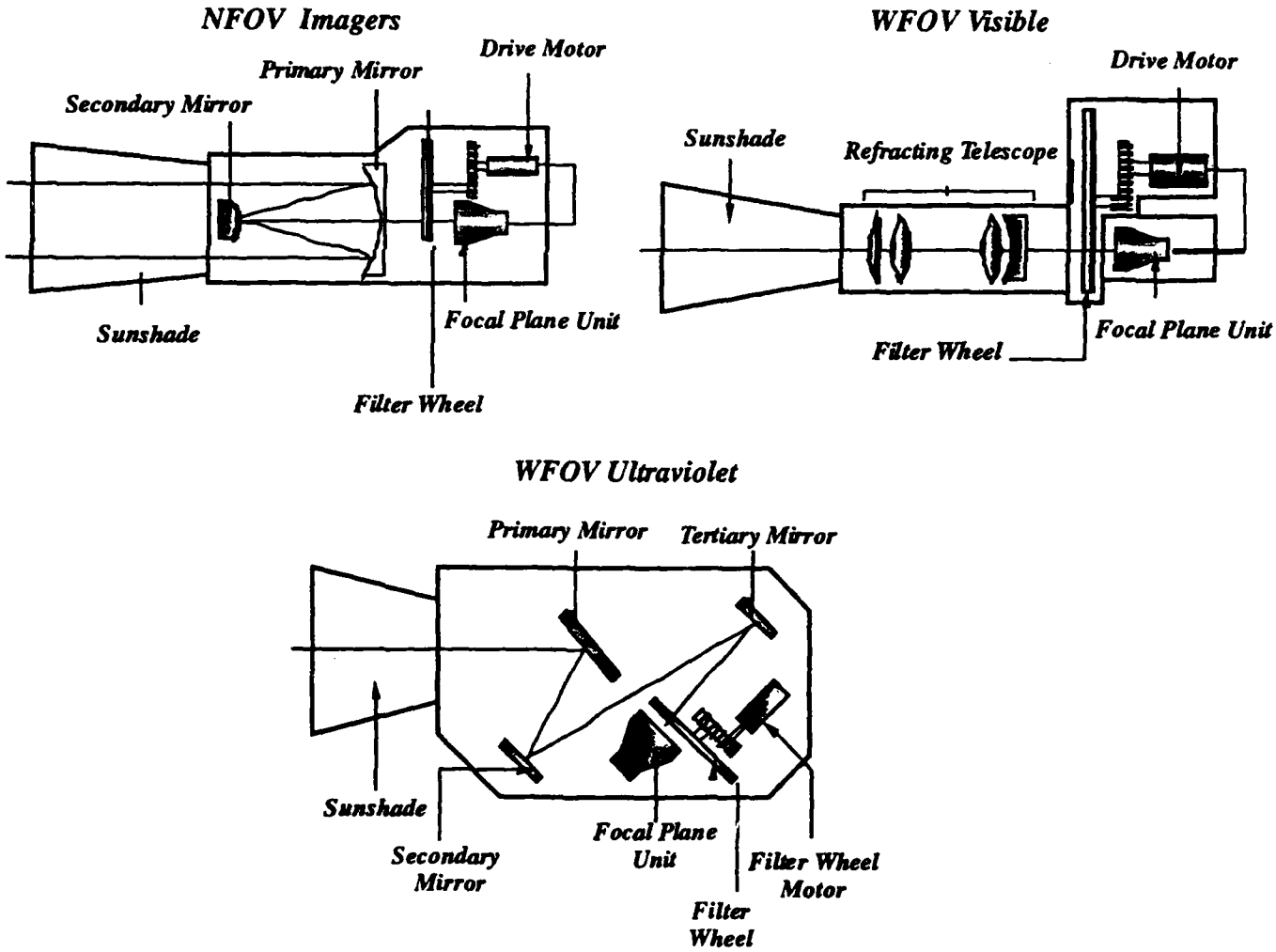

Fig. 3. Schematic diagrams of the three types of UVISI imagers

Figure 5 illustrates the concept of the UVISI spectrographic imaging. The scan mirror sweeps the slit through 1° in discrete steps of 0.10° or 0.05°. The step size of the mirror scan can be programmed to be 0.05° or 0.10°, corresponding to the slit size. The long dimension of the slit is also 1° and corresponds to the spatial dimension of the focal plane. The second dimension of the focal plane corresponds to the spectral or dispersive dimension of the spectrograph. The CCD can be programmed to sum counts on-chip so as to give several combinations of pixel sizes in both the spatial and spectral dimensions. Specifically, the CCD array can have 272, 136, or 68 pixels in the spectral dimension and 40, 20, 10, or 5 pixels in the spatial dimension. The particular combination chosen depends on the telemetry mode of the spacecraft and on the scene being viewed.

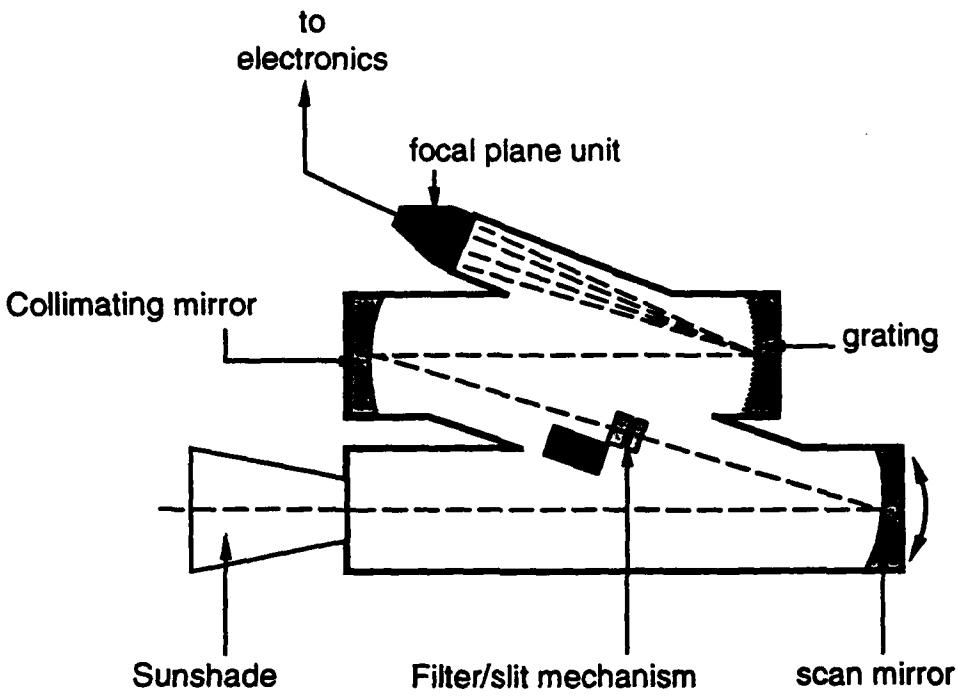

Fig. 4. Schematic diagram of a UVISI spectrographic imager (SPIM).

5. FOCAL PLANE UNITS

Each UVISI sensor has a focal plane unit with a common design, as shown in Fig. 6. (The design differs only in photocathode material.) Incident light stimulates photoelectrons in the photocathode material, and the photoelectrons are cascade-amplified by a chevron micro-channel plate (MCP). The amount of amplification or "gain" can be adjusted by changing the voltage across the MCP. The amplified electrons strike a green phosphor, which produces green light that travels down a fiber-optic taper to a charge-coupled device (CCD). The CCD converts the green light photons into digital signals.

The CCD provides an interscene dynamic range of 12 bits or about 4×10^3. Through the variation of the MCP voltage and its cycle time, the image intensifier provides an additional interscene dynamic range of about 10^5. At its highest gain, the focal plane unit operates in a photon-counting mode in which four pixel output words ("counts") represent one photo-event at the photocathode. The CCD outputs a maximum of 256x244 pixels for the imagers and 272x40 pixels for the spectrographic imagers. The intensifier gain is selected automatically based on the counting statistics of the raw image; however, the gain state can be overridden by manual command.

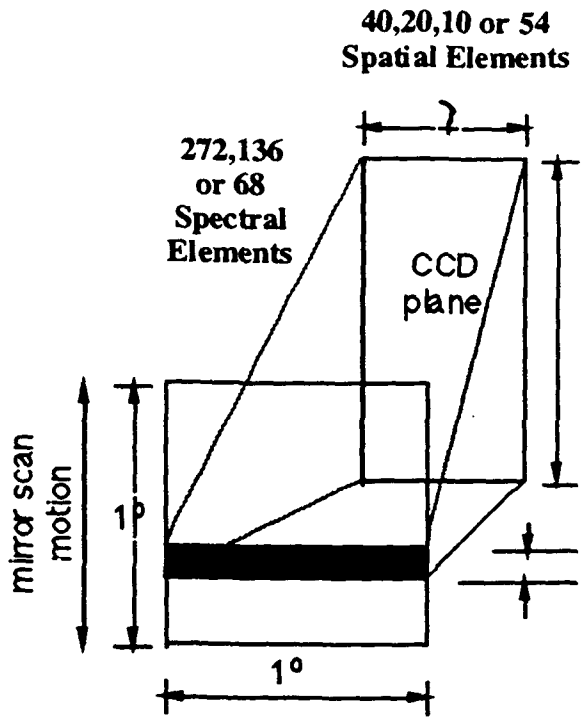

Fig. 5. Schematic of how spectrographic imaging works in UVISI SPIMs.

6. WAVELENGTH COVERAGE

Figure 7 graphically illustrates the wavelength coverage of the nine UVISI sensors. Each rectangular block indicates the full bandwidth of one sensor. The top grouping shows the imagers and their five effective filters; the bottom grouping shows the full dispersion of each SPIM. The filters have been chosen to select wavebands of scientific interest. In addition, the WFOV visible imager (IVW) has a near-focus filter that allows examination of small particles (self contaminants or co-orbiting debris) at ranges of a few meters in front of the spacecraft. The NFOV ultraviolet imager (IUN) has a filter at 290 nm that also has polarization properties that allow examination of polarized light. Certain SPIM slit positions have, in addition to blocking filters, filters that attenuate unwanted light within the bandwidth of the sensor. For example, SPIM1 has a filter that attenuates unwanted Lyman alpha radiation (121.5 nm) and OI radiation (130.4 nm), while allowing passage of LBH-band photons (>140 nm).

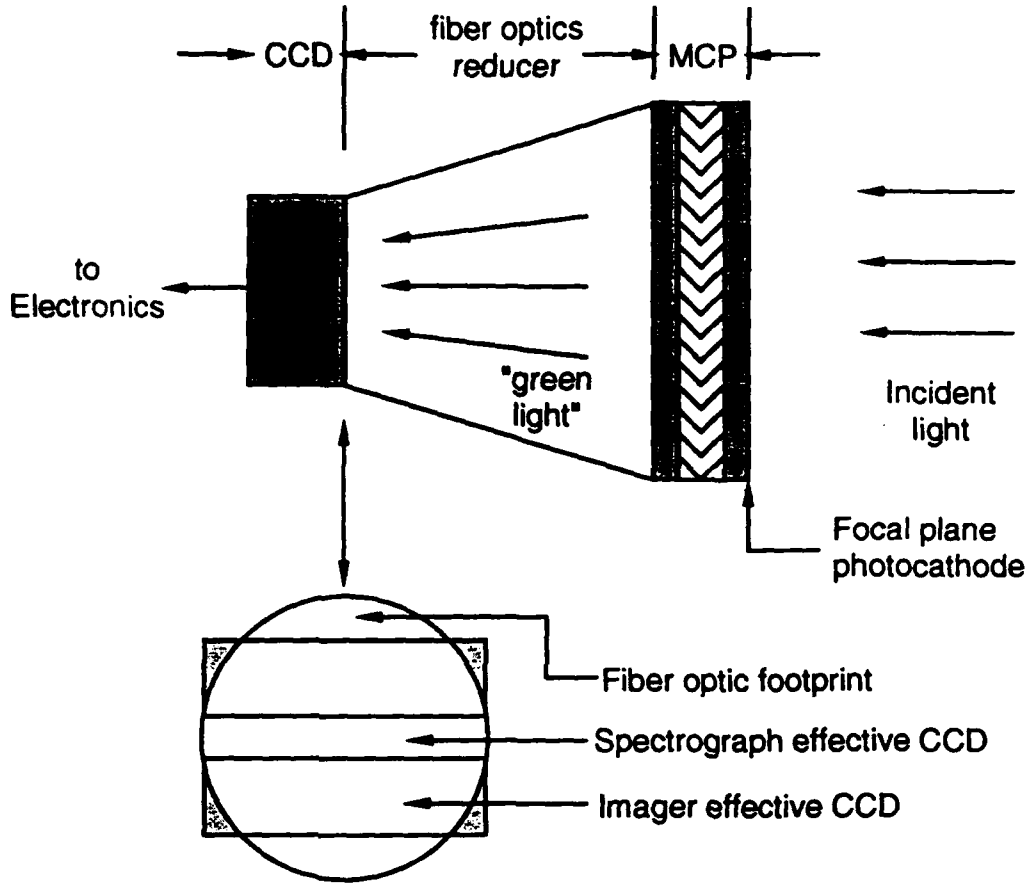

Fig. 6. Schematic diagram of UVISI focal plane unit. Focal plane units differ only in material of photocathode.

7. IMAGER SENSITIVITY

The purpose of this discussion is to address the suitability of the UVISI instruments to acquisition and tracking of RSOs at both the visible and solar blind UV wavelengths. A complete discussion of the UVISI instrument sensitivity as calibrated can be found in the series of calibration reports (one for each sensor) produced by the Johns Hopkins University Applied Physics Laboratory[12].

Figure 8 is a graphic demonstration of the inherent utility of a UV sensor in detecting objects near the hard earth or in earth limb. These data were collected by an imaging instrument flown on a LEO satellite. The instrument and telescope were of similar design to the UVISI IUN. The object in the image field is seen in reflected sunlight at a wavelength of 230 nm and is easily detected even against the relatively bright Earth limb background. The range to the object was ~1500 km at the time that this image was collected.

Although all nine UVISI instruments have potential utility to a space surveillance application, the two instruments of primary interest to this community are the IVN and the IUN narrow field of view ultraviolet and visible imagers. Figures 9 and 10 display the level of sensitivity required by the IVN and IUN imagers to detect a $1m^2$ plate as a function of range and of wavelength. The plate is assumed to be lambertian and have a reflectance of 0.8.

The curves show the intensities of reflected sunlight convolved with each wavelength band for each of the various filters. The horizontal lines represent the imager sensitivity at that particular wavelength. Thus, the intersection of a curve with its respective sensitivity represents the range expected for which a $1m^2$ object can be detected at a given wavelength.

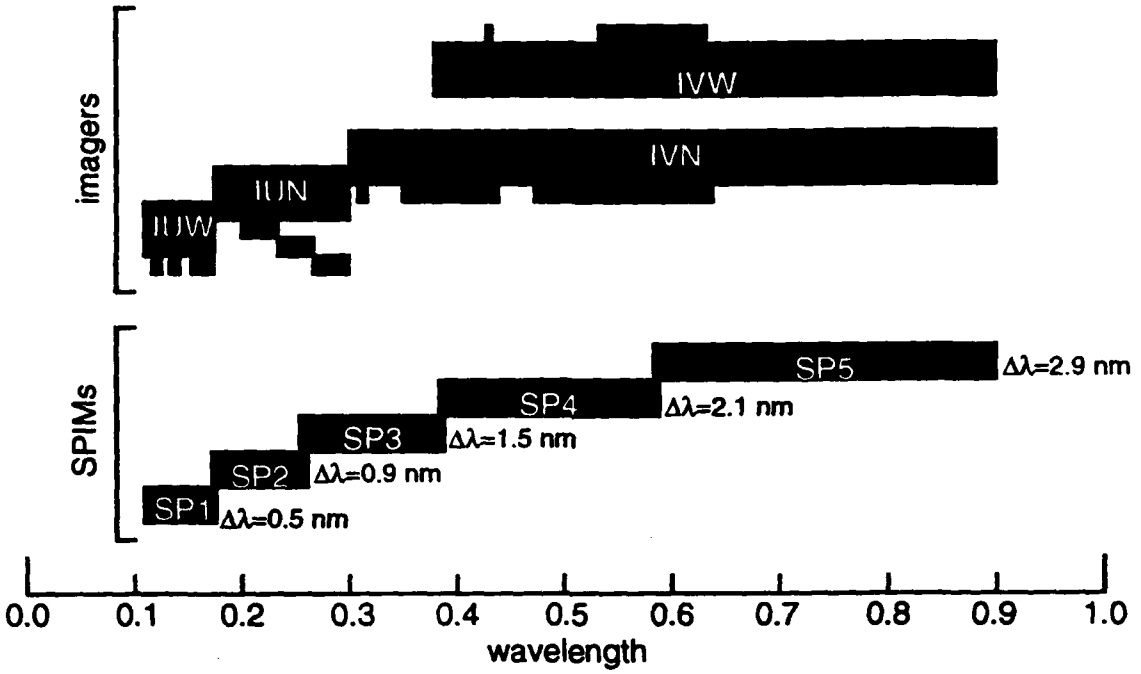

Fig. 7. Wavelength coverage of each UVISI sensor.

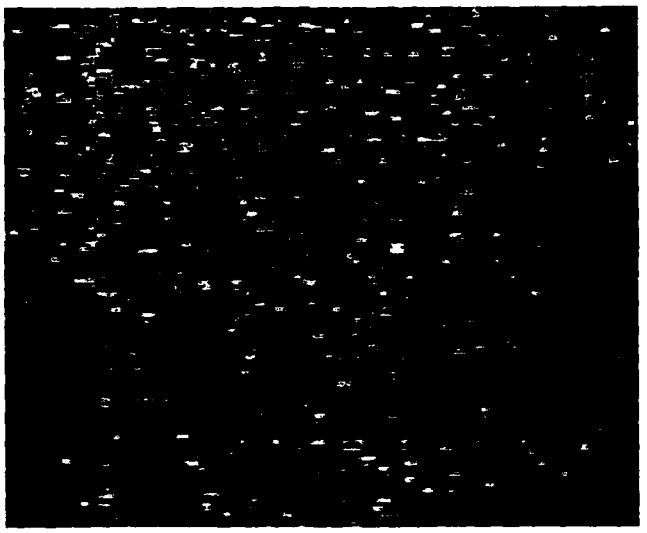

Fig. 8. Raw Image of a large RSO from space. λ=230 nm range ~1500 km. The background is sunlit earth limb.

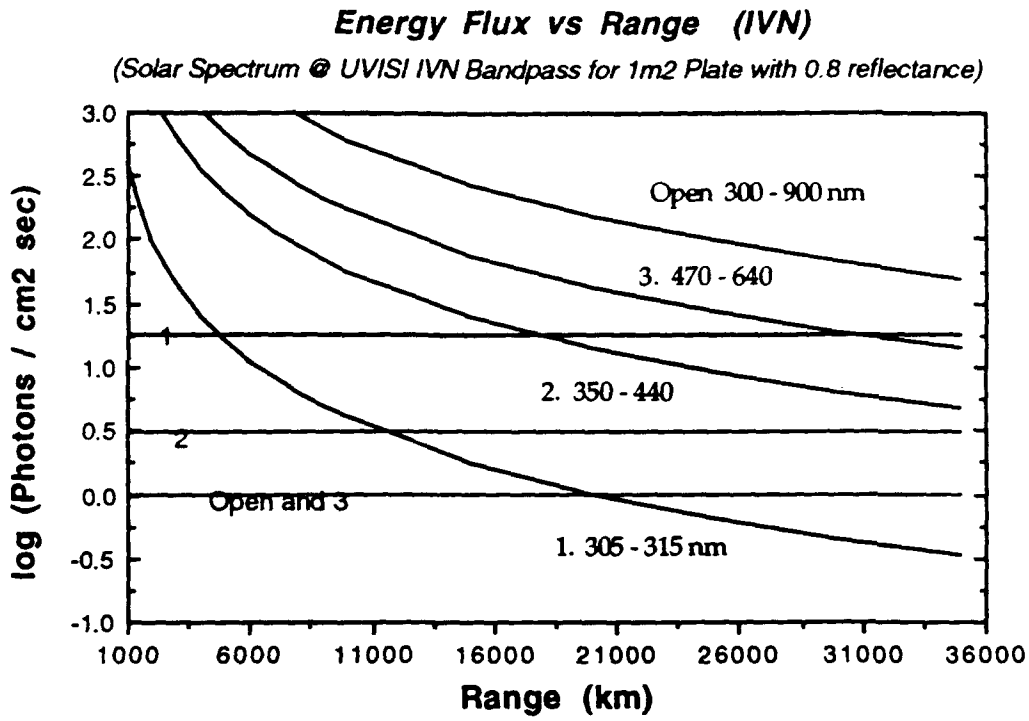

Fig. 9. Intensity of reflected sunlight vs. Range of a 1 m^2 plate with an albedo of 0.8. λ is binned to the IVN filter bands and the respective sensitivity is shown by horizontal lines .

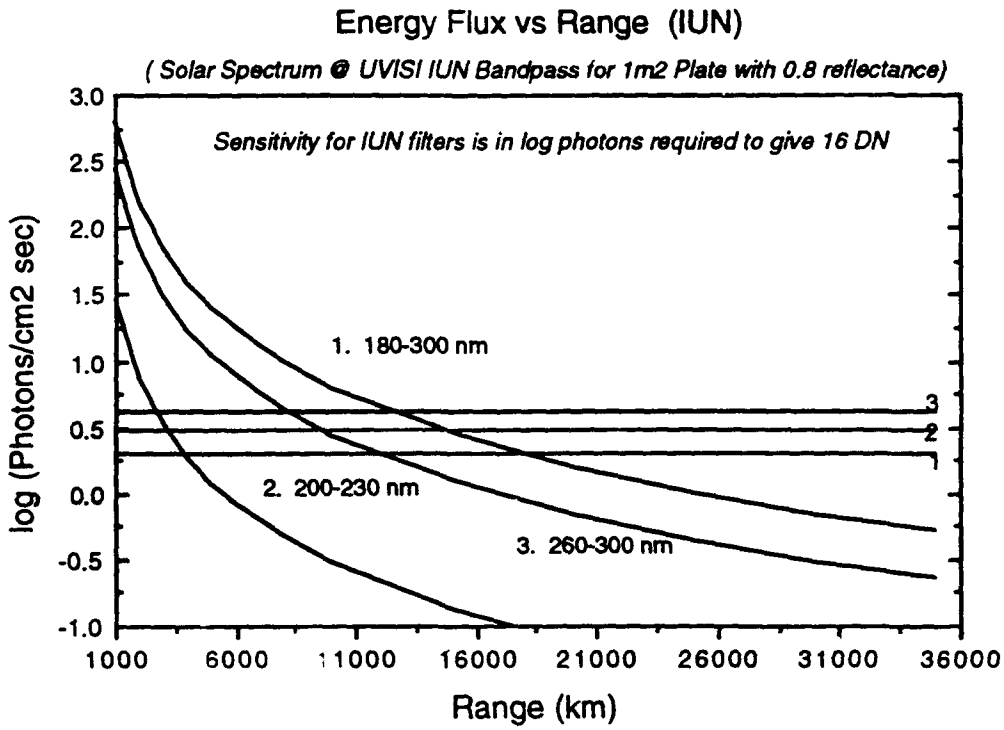

Fig. 10. Intensity of reflected sunlight vs. Range of a 1 m^2 plate with an albedo of 0.8. λ is binned to the IUN filter bands and the respective sensitivity is shown by horizontal lines .

Figure 9 shows that the IVN Open (300-900 nm), 2 (350-440 nm) and 3 (470-640 nm) filter positions can detect a $1m^2$ plate which lies beyond geosynchronous orbit. In the filter 1 (305-315 nm) position IVN is limited to a range of ~ 6000 km for detection of the same $1m^2$ plate.

Figure 10 shows that the detection range for the filter positions of the IUN varies with wavelength from ~ 20000 km for filter 1 (180-300 nm), about 15000 km for filter 3 (260-300) and falls off to ~ 4000 km for filter 2 (200-230 nm).

8. IMAGE PROCESSOR

The image processor of UVISI makes the instrument unique among those flown to date. The image processing system can acquire and isolate likely targets in an image FOV and communicate their positions to the MSX flight processor, which in turn points the satellite in a "closed-loop" fashion. "Target" can refer to either a point source such as a star or other satellite or to an extended source such as an auroral or cloud-top feature. The image processor operates in real time and can automatically select the operating mode of the UVISI imager based on its results.

The image processor accepts raw image data (a 256x244 pixel array of counts) from any one of the UVISI imagers. Processor software performs initialization and tracking functions that include filtering, smoothing, thresholding, and centroiding. The image processor seeks targets based on an *a priori* target description file containing weights for numerous target features such as size, shape, brightness, and location. The image processor then transforms target locations from UVISI pixel coordinates to spacecraft coordinates and passes them to the MSX flight processor, which performs Kalman filtering of other targeting inputs to select "true" targets for observation.

The image processor offers considerable flexibility in its operation. The nominal processor program determines likely targets based on a feature file contained in its memory. The software maximizes target likelihood by weighting the features in the file. One can change target selection by changing the weights in the file. Thus, a star target would be weighted to optimize brightness and pointedness, while the active segment of an aurora arc would be weighted to optimize elongation of shape and orientation. Because more than a single target can appear in one frame of data, the image processor can accommodate up to 23 different targets at once.

UVISI's image processor will initially carry a default set of target description vectors, characterizing a representative set of targets by such properties as average brightness and eccentricity. For some of the targets and phenomena to be observed, these descriptions are not much more than educated guesses. During the early operations phase, analysis of UVISI's image data will provide guidance in developing better description vectors. These will be tested with the tracking processor to improve overall system performance.

9. TRACKING & TRACK PROCESSOR

The fundamental design driver of the MSX tracking system are the various observations to be made by the spacecraft sensors. Of these the most highly valued observations involve the launch of missiles and sounding rockets dedicated to the MSX mission. Other high priority targets include cooperative missile launches, Resident Space Objects, and reference objects to be deployed from canisters onboard MSX. Background observations of the Earth limb and calibration observations of stars will also be conducted. One additional observation which has elements of both background observations and target tracking is the autonomous tracking of auroral bright-spots as they develop and move through the polar limb.

The fundamental requirement that flows down to the tracking system from this observation set is therefore, to provide a continuous "best" estimate of target state at a rate compatible with the attitude control system's requirements, whether or not sensor data is provided to or used by the track processor.

In order to accomplish this, a loosely coupled, distributed processing approach to tracking architecture was chosen, partly because no single space-qualified processor was found to be capable of the total computational load, and partly to reduce developmental risk. Figure 11 is a block diagram that schematically represents the pointing control system. The shaded boxes focus on tracking and experiment control.

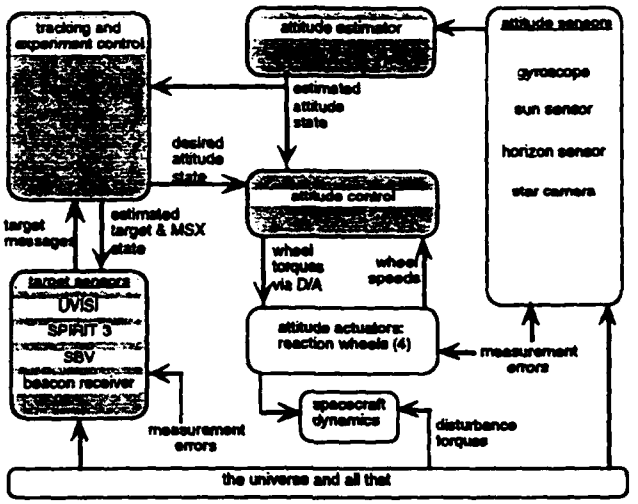

Figure 11 Spacecraft Pointing Control Architecture

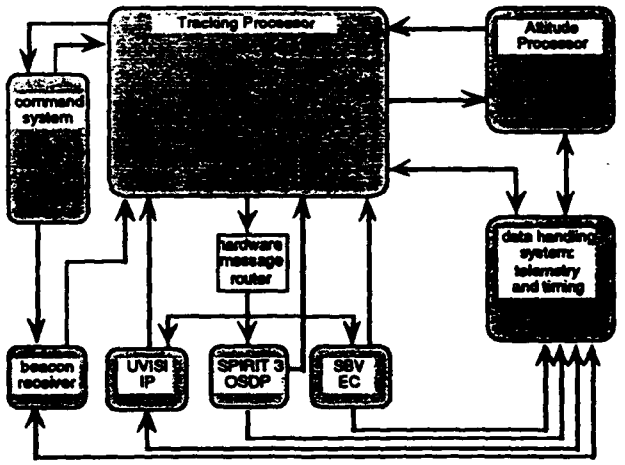

Figure 12 Tracking system Hardware Context

Figure 12 shows the hardware associated with tracking and the interfaces between the components. In this figure, each of the shaded boxes represents a spacecraft subsystem, and each arrowhead corresponds to a hardware interface. The boxes shown for the sensors are those parts of the sensor systems with direct interfaces to the tracking processor: UVISI's Image Processor, SPIRIT's On-board Signal and Data Processor, and SBV's Experiment Controller.

Tracking and Attitude Processors

The tracking processor and the attitude processor have identical central processing boards, built by APL around a Performance Semiconductor 1750A PACE chipset. The attitude processor has a dual-CPU-board system with a serial port between them. Each of the CPU boards has 256K words of error-detecting-and-correcting RAM, a 2 K word boot PROM, a memory management unit, and a processor interface circuit. An expansion board provides 256 K words of EEPROM used for storage of code, constants and data to be retained between power cycles. Also on the expansion board are an additional 256 K words of RAM and an interrupt expansion chip. The CPU is rated at 1.3 MIPS (DAIS mix with floating point) at 20 MHz clock rate. In addition to these boards, a variety of custom interface boards are in each computer chassis. Most of the custom interfaces are based on FIFO buffer circuits, with interrupts provided to the CPUs at the completion of a predetermined number of words for each interface. The tracking and attitude processors are fully redundant, as are all spacecraft life-critical subsystems.

Data Flow

Refer to figure 12 to follow the data flow through the tracking system. The attitude processor passes a time-tagged message to the tracking processor twice per second. The message contains the estimated attitude quaternion, attitude body rates and accelerations, the spacecraft orbital position and rate, and status information about the attitude processor. The tracking processor bases its response on control parameters received from the command system that describe the nominal trajectory. It returns to the attitude processor a time-tagged message with a desired attitude quaternion, rate and acceleration, and status information about the tracking processor. The rate for this message is also 2 Hz.

The desired attitude state may be based entirely on the nominal trajectory, or it may be based on sensor observations. To support the sensor observations, the tracking processor provides at 2 Hz a single message, broadcast by hardware to UVISI, SBV and OSDP. The message contains a target state estimate in Earth-centered inertial coordinates and again in UVISI-referenced coordinates (fractional pixels of the currently selected imager). The spacecraft attitude and orbit data from the attitude processor are also sent in the message, along with some information about the expected observational conditions of the target, and status information on the tracking processor. The messages from the sensors to the tracking processor are discussed below in the section "Closed-Loop Tracking."

Specification and Control of Data Collection

A data collection event may comprise any number of tracking events, with three perhaps typical (calibrate, observe target, calibrate). Each of these tracking events is described separately, and the parameters passed to the tracking processor include the start and stop times for each. While one event is executing, messages stored in the command processor memory may be transferred to the tracking processor, with start time for the new event preceding stop time for the current one. In this way an indefinite chaining of tracking events may be accomplished, with smooth transition from one to the next, and no return to parked mode in between. Blending of trajectories from the end of one event to the beginning of the next is the responsibility of operations team planners, not an on-board function.

Tracking event control parameters are broken into three categories: those that are usually constant, like sensor alignment matrices; those that define the next event, such as the nominal trajectory; and those that are intended to change the way the current event is being executed such as a revision to the choice of sensors to be used for tracking the current target. Any of these parameters may be sent in real time, but generally the parameters will be stored in the command system for delivery to the tracking processor at predetermined times.

When control parameters are sent, they may be stored in EEPROM to become the new defaults. Then whenever the tracking processor is rebooted, it will load those control parameters. Alternatively, the parameters may be stored only in RAM, and their values will be lost when the processor is turned off after the event. If an experiment's control parameters are stored in EEPROM, the processor may be

turned on by stored command even if it out of view of any ground station, and the experiment can be run without any real-time contact with the tracking processor.

Tracking Modes

Many data collection events do not require, or could not use, sensor data to improve pointing control. All that is needed is a specification of the desired maneuvering as a function of time, i.e. open loop. The sensors then send their data to the tape recorder, but no use is made of it on board. While this kind of tracking event is simpler than a closed-loop track, there are still many options. Furthermore, any closed-loop tracking event requires a nominal trajectory as the basis for the track and to specify where the target is to be acquired 14 .

When there is a sufficiently detectable, compact target, especially one whose dynamics are known fairly well, closed-loop tracking can be used to advantage. UVISI and the tracking processor cooperate in closed loop target tracking. The UVISI image processor examines a single frame from one of its four imagers, and sends to the tracking processor a rank-ordered list of the objects it detects. The frame rate, and the message rate, is 2 Hz. The objects are ranked according to their goodness-of-fit to a feature vector uplinked to the image processor.

The list of potential targets from the image processor may be used in either of two ways, as specified by experiment control parameters. The tracking processor may be instructed simply to use the object ranked highest by the image processor that is within a reasonable distance of the estimated target location. On the other hand, the tracking processor can use its velocity filtering algorithm to choose that object in the list that most closely matches the velocity profile of the target, using the image processor's rankings to break ties. This is used for star removal.

The type of closed-loop tracking to employ depends primarily on the *a priori* knowledge of target dynamics. If little or nothing is known about the forces governing target motion in advance, then it is appropriate to use the alpha-beta tracker. This algorithm predicts the future location and velocity of the target by assigning weight *alpha* to the position, *beta* to the velocity, and linearly propagating the state in these two variables. This algorithm is sometimes called a "data follower," because it accumulates no confidence in its predictions based on diminishing error, and uses no underlying model of the target's dynamics. It has minimal risk of diverging from the target unless the sensors stop providing reasonable data, or target dynamics exceed spacecraft slewing capabilities, but it has very little ability to follow the target through extended data dropouts.

A second method, the extended Kalman filter, bases its state propagation on underlying equations of motion for the target. As sensor data is received, the model's state vector is corrected to minimize differences between it and the observed state. When the predicted state agrees closely with the sensor data, confidence is increased that the state vector convergence is good. With injudicious setting of the filter gains, convergence time may be artificially increased, or, in the catastrophic case, sensor data may be rejected in favor of erroneous model predictions, and the filter may actually diverge.

With the proper settings, however, an extended Kalman filter can smooth sensor noise effects, minimize the effects of "wild points," and propagate target state accurately through times of sensor data dropout. Particularly when the target dynamics are very well known, as in ballistic motion, the Kalman filter can effectively correct wrong initial assumptions about the target's position and velocity, converging to a state vector that minimizes sensor data residuals.

If closed loop tracking is to be performed, one or more sensors must be selected. The tracking processor may be commanded to use one sensor until and unless it loses the target, and then switch to the next priority sensor, or it may be told to give two or all three of the sensors the same priority. If two or more sensors are selected for simultaneous use, sensor fusion is specified. When incorporating sensor

data using either the Kalman filter or the alpha-beta tracker, it is effectively weighted by its frequency of arrival, in the sense that each data point from a source is given equal weight, without regard to its rate.

Loss of track by all selected sensors leaves the tracking processor with two choices: continue to propagate the last predicted target state, or revert to the nominal trajectory. The decision is made in advance by spacecraft operators. Note that the tracking processor may be operated in either alpha-beta track or in Kalman filter mode while the spacecraft is pointed inertially. In this mode of operation target track files can be collected on objects which pass through a sensor's field of view and at each loss of track a new target will be selected.

Sensor Fusion

Data from very different sensors may be combined into a single target state estimate. There is much to learn about the process. When incorporating the sensor data into the prediction update, a model of sensor noise is applied. By increasing the expected-noise values for a particular sensor, the influence of the data may be decreased. Thus, by adjusting the noise models, same-priority sensors with different message frequencies can be equalized. For targets that have distinctive signatures in one spectral band, intuition says that the weight of corresponding sensor data should be increased. The MSX tracking system can allow us to examine this and other issues in multispectral sensor fusion.

Another way to use multiple sensors for one tracking event is to switch from one to another at a predetermined time. Some phenomena may have definable points in their trajectories at which such a change of sensors is called for. For example, the accuracy provided by the beacon receiver are not as great as for UVISI. It may make sense therefore to start tracking a cooperating test vehicle with the beacon receiver, and then switch over to UVISI at some point in the vehicle's flight. For such highly valued targets, however, it is certainly advisable to quantify the benefits of this approach first.

Simulation

For testing of the tracking system software at higher levels of integration, a testbed simulator[3] was developed. The simulator provides full electrical-level compatibility at all tracking system interfaces, and varying degrees of fidelity in the data exchanged across them. It allows different degrees of hardware-in-the-loop simulation, including the tracking processor, attitude processor, beacon receiver, and UVISI image processor. The simulator has supported test generation, data capture and analysis throughout the development effort, and will be used after launch for system characterization and software maintenance.

10. SUMMARY

The preceding paper was meant to provide the reader with some insight into the capabilities of the UVISI Instrument coupled with its Image and Track processors. It is clear that target selection, track file computations and trajectory determination can be accomplished in a variety of ways and at various different wavelengths. The UVISI Narrow Field Imagers are best suited to collect track data on RSOs at ranges up to and beyond geosynchronous. The overall dynamic range of ~10^5 and the solar blind UV wavelength range allows UVISI to view RSOs and other dim objects in deep space as well as objects in the earth limb or against a sunlit earth background. When coupled with the MSX tracking and control system, UVISI has the potential to acquire and track RSOs providing necessary track file information and long duration exposures. Spectral information from the SPIMs could thus be collected and contribute to multispectral SOI by the identification of specific reflectance spectra.

11. ACKNOWLEDGMENTS

The authors would like to thank the large number of supporting engineers and scientists who contributed to the development and construction of UVISI and the Image and Track Processors. The UVISI instrument and the MSX mission receives funding through the Ballistic Missile Defense Office, formerly the Strategic Defense Initiative Organization.

9. REFERENCES

1. C.-I. Meng and R .E. Huffman, "Ultraviolet imaging from space of the auroral under full sunlight," *Geophys. Res. Lett., 11*, 315-318, 1984.
2. F. W. Schenkel and B.S. Orgorzalek, "Auroral images from space: Imagery, spectroscopy, and photometry," *APL Tech. Dig. 8*, 309-317, 1987.
3. A.F. Davidson, K.S. Long, S.T. Durrance, W.P. Blair, C.W. Bowers, S.J. Conard, P.D. Feldman, H.C. Ferguson, G.H. Fountain, R.A. Kimble, G.A. Kriss, H.W. Moos, and K.A. Potocki, "The Hopkins Ultraviolet Telescope: Performance and calibration during the Astro-1 Mission," *Astrophys. J. 392*, 264-271, 1992.
4. M. D. Griffin and M. j. Rendine, "Delta 180/Vector Sum: the first powered space intercept," *AIAA 26th Aerospace Sciences Meeting, Reno, NV, January 1988.*
5. B. B. Holland, J. C. Ray, and A. J. Green, "Delta 181, the Thrusted Vector Mission," *AIAA 27th Aerospace Sciences Meeting, Reno, NV, January 1989*.
6. P. F. Bythrow, J. F. Carbary and R. E. Gold, Delta Star Target Observations at Wavelengths < 1μm, *Proceedings of the Short Wavelength Phenomenology Conference JHU/APL June 1990*.
7. S. C. Solomon, P. B. Hays, and V. J. Abreu, "Tomographic inversion of satellite photometry," *Appl. Opt., 19*, 3409-3418, 1985.
8. R. R. Meier, "Ultraviolet spectroscopy and remote sensing of the upper atmosphere," *Spcce Sci. Rev., 58*, 1-185, 1991.
9. D. J. Strickland, R. Link, and L. J. Paxton, "Far-UV remote sensing of thermospheric composition and the solar EUV flux," in Ultraviolet Technology IV, R. E. Huffman, ed., *Proc. Soc. Photo-Opt. Instr. Eng., 1764*, 117-131, 1992.
10. D. J. Strickland, J. R. Jasperse, and J. A. Whalen, "Dependence of auroral FUV emissions on the incident electron spectrum and neutral atmosphere," *J. Geophys. Res., 88*, 8051-8062, 1983.
11. R. C. Henry, J. Murthy, M. Allen, M. Corbin, and L. J. Paxton, "Spectroscopy and imaging of the cosmic diffuse UV background radiation," in Ultraviolet Technology IV, R. E. Huffman, ed., *Proc. Soc. Photo-Opt. Instr. Eng., 1764*, 61-71, 1992.
12. J. F. Carbary The UVISI Calibration Report, *JHU/APL Publication 1994*.
13. L. Lee Pryor and Daniel S. Wilson, *MSX Flight Software Test Bed*
14. R. L. Waddell Jr., P. K. Murphy and G. A. Heyler, Image and Track Processing in Space, Part 1, *Proc. of the AIAA conference on Computing in Aerospace, pp. 576-585 Oct. 1993.*

The SBV Sensor Emulator: A High Fidelity Focal Plane Simulator

Thomas P. Opar (MIT Lincoln Laboratory)

1.0 Introduction

The Space Based Visible (SBV) sensor on the Ballistic Missile Defense Organization Midcourse Space Experiment (MSX) satellite collects and processes image data from a staring, CCD array. As an aid to visualization of the images, provide test cases for software and algorithm development, and to serve as the basis for phenomenology modelling, the SBV Sensor Emulator has been developed. The purpose of the SBV Sensor Emulator is to provide the SBV user community with high fidelity, simulated images. The SBV program is already rich in field measurement from an SBV-like sensor which provides one set of opportunities to test software. The existing field test data is useful for assessing the functionality of existing software, but does not provide a complete software assessment due to the differences between the existing collection systems and SBV. There are six primary differences which are specifically addressed by the SBV Sensor Emulator, which are:

1.) The spatial structure of the multiplicative fixed pattern due to optical and CCD effects is not present in the field data.
2.) The SBV sensor has a large degree of optical distortion which is absent in the current field data.
3.) The noise performance is a sensor characteristic which is unique to each individual sensor.
4.) The spectral response of the sensor differs from previous measurements, primarily as a result of the SBV mirror spectral reflectance.
5.) The Optical Point Spread Function (PSF) is sharper than most of the field test data and varies across the focal plane.
6.) The SBV Sensor is space-based and opens a variety of background phenomenology and encounter RSO encounter geometries which are not accessible from the earth. For example, the dominant background contribution for low tangent altitude observations is from Non-Rejected Earth Radiance (NRER) which is absent from existing data.

The SBV Sensor Emulator provides the means to alleviate the deficiency in the available field test data by utilizing the extensive set of ground calibration and characterization data to provide the means to create high fidelity, SBV-like images for the MSX/SBV software users and developers.

2.0 SBV Sensor Emulator Overview

Since this emulator is being designed specifically for the SBV sensor an important caveat should be noted. The SBV sensor is designed primarily for above - the - horizon (ATH) observations only. This design implies that the emulator need only include ATH background contributions.

The current implementation of the SBV Sensor Emulator includes four major components:

1. Cover Closed (Dark) Frame Simulation
2. Extended Source Background Modelling
3. Stationary and non-Stationary Point Target Simulatior
4. Analog - to - Digital Conversion

The output from the emulator is consistent with existing SBV data processing software. It produces files which are in the format used by the SBV CONVERT software, the SPOCC

Processing Pipeline, and the SBV Performance Assessment Team software.

This paper reviews the four major components of the emulator. The purpose of this paper is to provide an overview of the features and capability of the emulator. The mathematical formulation of the various elements is presented in the following sections. Section 3 provides details on the Cover Closed or Dark Frame Simulation. Section 4 is a review of the Extended Source Modelling. The techniques to generate point sources on the focal plane are addressed in Section 5. The simple Analog - to - digital conversion routine is described in section 6. Section 7 presents the summary and conclusions.

3.0 Cover Closed (Dark) Frame Simulation

The emulator begins by creating the contributions from the Zero Correction, the Dark Current, and the noise. The Zero Correction is the parameter which is used to set the DC bias level in the camera. The DC bias level at the output is termed the Zsum and corresponds to the mean signal level in a pixel with no photons applied. The Zsum is a function of the Zero Correction and it's value depends on the specific camera chosen. (The SBV sensor has two independent, redundant camera Each is supported by the emulator.) The program begins by setting the signal level in each frame to the Zsum. This is done as a noiseless process and the actual operation is depicted by Equation 1.

$$S_{ij}^{n} = \text{Zsum (ZC,Camera)} \qquad 1.)$$

where

S_{ij}^{n} = Signal in pixel (i,j) for frame number n
ZSum = Signal level for zero photons as a function of the Zero Correction and the Camera

The relationship between Zsum and Zero Correction is linear and can be written as

$$\text{Zsum} = \text{Zsum}^{0} (\text{ZC} - \text{ZC}_{ref}) \qquad 2.)$$

Table 1 lists the set of these parameters which was derived from the SBV characterization. One set of parameters is supplied for each of the SBV camera halves.

Table 1
Model Parameters for the Zsum Dependence on Zero Correction

Camera	$Zsum^0$	ZC_{ref}
A	7.93	120.7
B	7.84	121.6

After the Zsum value has been added to the pixel, then the dark current signal is added. The dark current signal depends on the exposure time, while the dark current is a function of the focal plane temperature. The dark current signal also exhibits a fixed pattern behavior in which case the average dark current varies pixel - by - pixel. The focal plane distribution of dark current is represented by a two-dimensional 420 by 420 array for each of the four CCD arrays. The dependence on focal plane temperature is set by an empirical model. The dark current model is explicitly defined in Equation 3.

$$D_{ij}^{n} = DM_{ij}\, e^{C_{ij}^{k}\left(T_{FPA} - T_{FPA}^{ref}\right)} \frac{T_{Exp}}{T_{Exp}^{Ref}} \qquad 3.)$$

where

D_{ij}^{n}	= Dark Current signal in pixel (i,j) in frame n
DM_{ij}^{k}	= Dark Current in pixel (i,j) on CCD # k
C_{ij}^{k}	= Temperature correction parameter for CCD#k and pixel (i,j)
T_{FPA}^{re}	= Reference focal plane temperature (°K)
T_{FPA}	= Focal Plane Temperature (°K))
T_{Exp}^{Ref}	= Reference focal plane exposure time (s)
T_{Exp}	= Focal plane exposure time (s)

The temperature correction parameter is set to a constant across all CCDs and pixels in this version.
The final contributor to the cover closed signal is the noise. The dark noise has two contributions one is from the Poisson Noise due to the dark current signal and the other is the sum of all other electronic noises in the system. In this version of the emulator the dark noise is modeled by a zero-mean Gaussian distribution. The variance of the noise is assumed to be a constant value and is seat to rms value equaling 5.0 electrons at high gain. The model is implemented according to equation 4.

$$S_{ij}^{n} = S_{ij}^{n} + \Gamma(0, \sigma_{ij}) \qquad 4.)$$

where σ_{ij} is the standard deviation of the noise in the pixel (i,j) and $\Gamma(\mu,\sigma)$ represents a Gaussian random variable with mean μ and standard deviation σ. The noise value is determined by the root sum of squared values of the Dark current Poisson Noise and the system noise:

$$\sigma_{ij}^{2} = \sigma_{sys}^{2} + D_{ij} / g \qquad 5.)$$

where

σ_{sys}^{2}	= system noise level in digital numbers
D_{ij}	= dark current signal in pixel (i,j)
g	= system transfer function or gain (photo-electrons / digital number)

The relationship between dark current signal and the noise is derived from the assumption that the process is defined by Poisson statistics.

4.0 Extended Source Background Modelling

The SBV Sensor Emulator currently includes three primary background constituents; diffuse galactic backgrounds, Out-of-Field-of-View Radiance (OFVR) backgrounds, and discrete celestial point sources. This section details the modelling of the first two of these contributions. The last is described in Section 5.

4.1 Diffuse Galactic Background

The signal in a pixel due to a extended source background feature that fills the pixel is written in the following form

$$B_{ij} = A_{ij}^{Eff} qe_{ij} \tau^{Optics} N_0 10^{-0.4 B_{vm}} \alpha_{ij}^2 T_{Exp} \qquad 6.)$$

where

B_{ij} = signal in the pixel (i,j) due to the extended background source
A^{Eff}_{ij} = effective aperture area for the pixel (i,j)
qe_{ij} = solar weighted quantum efficiency for the pixel (i,j)
τ^{Optics} = optical throughput of the sensor
N_0 = zero magnitude flux
B_{vm} = background visual magnitude per arcsec^2
α_{ij}^2 = pixel steradiancy (arcsec^2)
T_{Exp} = frame exposure time

The celestial background in the SBV Emulator assumes a constant background visual magnitude across the focal plane. This diffuse background component is primarily a function of the galactic latitude. It is due to the signal from unresolved stars and extended features. Table 2 provides an estimate of the diffuse galactic background for the SBV sensor.

Table 2
Diffuse Galactic Background Magnitude vs. Galactic Latitude

Galactic Latitude (degree)	Bvm (mag / arcsec^2)
± 5	22.2
± 30	24.0
± 60	25.0

The background level for which the Poisson noise in the background equals the sensor noise is 22.2 magnitudes / arcsec^2.

The product $A^{Eff}_{ij}\ \alpha_{ij}^2$ is a function of the design of the sensor. The SBV sensor has structure introduced from each of these factors. The structure in the multiplicative map is primarily due to two aspects of the off-axis design of the SBV sensor. First, the effective aperture area of the telescope varies across the focal plane. This "pupil distortion" produces a radial structure in the map centered on the on-axis point. Secondly, the f/number of the telescope varies from point - to - point. The variation in f/ number causes the pixel steradiancy (α_{ij}^2) to be smaller in one portion of the focal plane with respect to another. Thus when illuminated by a uniform source there is a gradient in the signal on the focal plane.

4.2 OFVR Backgrounds

The primary component of the background for low earth satellite observations may be due to OFVR contributions, most notably the NRER. One component of the NRER is directly related to mirror contamination. Quantification of the contamination, via measurements of the Bi-directional Reflectance Distribution Function (BRDF) of the SBV mirrors, has been made over a long period. The BRDF data can be used to compute the expected NRER background as function of tangent altitude for a fully illuminated earth. In the SBV Sensor Emulator the NRER is modeled by allowing the quantity Bvm in Equation 6.) to be a function of the tangent altitude. Table 3 is listing of the expected NRER background visual magnitude at various tangent altitudes, along wiected signal level in electrons for a 0.4 s exposure. These values are expected to change on orbit.

Table 3
Expected NRER Background

Tangent Altitude (km.)	NRER Bvm (vm / arcsec2)	Signal (electrons)
100	15.4	4970
190	16.2	2380
280	16.9	1250
360	18.2	377
435	18.9	198
505	19.2	150
565	19.4	125
630	19.7	95
680	20.2	60

5.0 Stationary and non-Stationary Point Target Simulation

The Point Target Simulation is one of the most critical features of the SBV sensor emulator. It supports a number of critical phenomena characteristic of the staring focal planes sensors. These features which the Point Target Simulation include are:

1.) The temporal statistics of a point source target obey Poisson Statistics.
2.) The optical spread function is described by a two-dimensional Guassian distribution function whose parameters vary across the focal plane.
3.) The pixel - to - pixel response and effective aperture are vary across the focal plane.
4.) The entire pixel area may not be active, that is some portion of the pixel may not electrically respond to photons.
5.) Motion of the point target due to encounter geometry, drift or jitter, and/or tracking.
6.) Optical distortion

The manner in which these features are implemented through an event driven implementation of the Point Target Signal Model. The "event" is the arrival of a photo-electron on the focal plane. Each photo-electron produced at the focal plane from the point source is handled independently. This allows for the straightforward implementation of these six features.

This Point Target Simulation is a numerical estimation of the equation which explicitly

describes the signal in a pixel due to a point target moving across the focal plane.

$$S_{ij} = A_{ij}^{Eff}\, qe_{ij}\, \tau^{Optics} \int_0^{T_{Exp}} dt\, N_0\, 10^{-0.4\, T_{vm}(t)} \iint_{pixel\ (i,j)} dx\, dy\ \ PSF_{ij}\,(x(t), y(t)) \qquad 7.)$$

The Point Target Simulation is outlined if Table 4. A pseudo-code representation of the algorithm is provided. A brief description of some of the important steps in the simulation provides some insight into it's implementation.

Table 4
Point Target Simulation
(Event Driven Simulation)

1. Initialize the time to zero (t = 0.)
2. While the time is less than the Exposure Time...
   - 2.1 Compute the Mean Generation Time of Photo-electrons
     - 2.1.1 $\tau_0 = 1./Sdot\,(t)$
   - 2.2 Compute the arrival time of the next photo-electron based on the mean rate τ_0
     - 2.2.1 $\tau = -\tau_0 \ln(U_1)$, where U_1 is a uniformly distributed random number
   - 2.3 Update the time $t = t + \tau$
   - 2.4 Compute the position of the center of the PSF on the focal plane
     - 2.4.1 $x_{FP} = x(t)$
     - 2.4.2 $y_{FP} = y(t)$
   - 2.5 Use the Gaussian PSF assumption and place the photo-electron with respect to the center of the PSF.
     - 2.5.1 $x_{FP} = x_{FP} + \sigma_x(x_{FP}, y_{FP})\, G(0,1)$
     - 2.5.2 $y_{FP} = y_{FP} + \sigma_y(x_{FP}, y_{FP})\, G(0,1)$
   - 2.6 Integerize the position focal plane position
     - 2.6.1 $i = fix(x_{FP})$
     - 2.6.2 $j = fix(y_{FP})$
   - 2.7 Check to see if the photo-electron falls in an active region of the detector and if so add the signal to the image
     - 2.7.1 if $|x_{FP} - i| \le fill_x$ and if $|y_{FP} - i|\ fill_y$ then
       - 2.7.1.1 Signal in pixel (i,j) = Signal in pixel (i,j) + 1 + η_{ij}

   End of While Loop

Step 2.2 The term S_{dot} represents the average photo-electron production rate at the focal plane. Explicitly:

$$S_{dot} = A_{Eff}\, \overline{qe}\, \tau\, N_0\, 10^{-0.4\, T_{vm}} \qquad 8.)$$

where the terms are identical to those in Equation 6. except that the pixel - to - pixel variables are replaced by their averages. In addition

T_{vm} = target visual magnitude, defined as time independent parameter.

Step 2.3 This step insures that the total signal from a point target obeys Poisson statistics. The arrival time of the photo-electrons is assumed to be described by a negative exponential distribution function.

Step 2.4 The position of the target as a function of time on the focal plane x(t) & y(t) contains the effects of the motion of the target and sensor. If there is any jitter in the line of sight it is applied here. Also if the targets are tracked perfectly then these terms are exactly equal to the location of the center of the PSF. These quantities are in focal plane units, thus the optical distortion appropriate for the CCD is applied to get from Right Ascension and Declination to focal plane units. The Emulator utilizes a star catalog and a prescribed boresite Right Ascension and Declination to map the stellar background onto the focal plane.

Step 2.5 The program assumes that the Optical Point Spread Function is described by a two - dimensional Guassian function. For each photo-electron it's location is randomly assigned using a zero mean, unit variance (G(0,1)) Gaussian random number generator. The standard deviation of the Guassian varies across the focal plane, and is directly related to the Ensquared Energy. The relationship is:

$$Ensq = erf(fill_x \gamma_x)\ erf(fill_y \gamma_y) \qquad 9.)$$

where

Ensq = Ensquared Energy
erf(z) = error function of the argument (z)
$fill_z$ = pixel fill factor, which represents the portion of the pixel that is active. This quantity is set to 1.0 for the SBV sensor.

The parameter γ relates the standard deviation in equation 10 to the argument of the error function.

$$\gamma_z = \frac{1}{\sqrt{8}\,\sigma_z} \qquad 10.)$$

Step 2.7 This step incorporates a number of features. First of all, if the photo-electron falls outside the active region it is neglected. The signal is incremented only if the photo-electron falls on the active region. Secondly, the variation in quantum efficiency is applied at this point. The photon arrival rate is based on the mean quantum efficiency over the entire array. The term η_{ij} is defined as

$$\eta_{ij} = \frac{qe_{ij}}{\overline{qe}} - 1 \qquad 11.)$$

This insures that those pixels whose quantum efficiency exceeds the average produce more photo-electrons.

6.0 Analog - to - Digital Conversion

Up to this point the SBV Sensor Emulator performs it;'s calculations at the focal plane in photo-electrons. The output of the sensor however is a 12 -bit (0 to 4095) integer number. In order to complete the emulator some sort of Analog - to - Digital Conversion (ADC) must be performed. The simplest version of the ADC chain is currently implemented. In this case the electronic gain (the number of photo-electrons per digital number) is specified and is held constant over the entire sensor range. The signal in each pixel is divided by the gain and integerized. Values exceeding 4095 are clamped at 4095. Table 4 lists the gain states implemented as derived from the sensor ground characterization.

Table 4
Gain States in the SBV Sensor Emulator

Gain State	Electronic Gain (photo-electrons / digital number)
High	27.6
Low	6.37

7.0 Summary and Conclusions

A software emulation of the SBV sensor has been developed. It includes many of the critical features the SBV sensor which are not present in existing field test sensors. Most notably, optical distortion, the multiplicative fixed pattern noise, the sensor noise, the Point Response Function. Though it's primary purpose is for testing and evaluating software it should prove to be a useful tool for mission planning, data analysis, and algorithm development.

The version of the software described in this paper is the initial release. Further upgrading and enhancement of the emulator anticipated. Additional background features (earthlimb and Non-Rejected Solar) are planned. Gamma events, non-linear effects due to extremely bright target, and a realistic ADC model which allows for non-linearities are also planned. Finally, the point target model for RSOs does not include any time variation of the signal, this deficiency will also be removed.

Ground Based Infrared Observations of Space Debris

Dr. Michael L. Cobb, Naval Research Laboratory
Dr. Stephen H. Knowles, Naval Space Command

ABSTRACT

Using a 61" astronomical telescope and a single channel infrared bolometer, several space objects including orbital debris were observed at wavelengths of 10 and 20 microns. A total of 9 objects were observed, 4 of which were observed on 2 different nights. A combination of effective IR cross sections, bolometric temperatures, and emissivities were derived and compared with accepted radio values. An object with area of 4.2 m^2 at an altitude of 770 km was observed with signal to noise ratio of 600:1 in one second integration time. Bolometric temperatures ranged from 280-390 K°. Derived IR emissivities were consistent with accepted sizes except for 2 cases. These differences may not be significant however since simultaneous measurements were not obtained.

Current observations are used to predict minimum detection sizes of debris as a function of altitude and differential tracking velocity with this size telescope. If there are no differential tracking velocities then detection size is limited by integration time and sub cm sized objects can be detected. Differential tracking velocities near 10 m/s allow objects less than 10 cm to be detected. In surveillance mode (no velocity information) objects 1 m in size at 300 km orbits can be detected. Future high speed image processing hardware could reduce detection sizes by a factor of 10. Since IR observations are not effected by sunlight, observations 24 hours per day are possible guaranteeing space catalog updating upon demand.

I Introduction

There are several ways of detecting orbiting space objects including active and passive techniques in the radio and optical wavelengths. While considerable observational data exists for radar and visible observations, thermal infrared observations are less documented. The current status of radar and visible observations will be reviewed as well as the justification for studying space debris in general. Next the basic theory concerning the black body emission from objects is derived. An interesting set of observational data is then presented which confirms the expected sensitivities. A brief discussion of the results is followed by conclusions which point to future considerations that should allow objects 10 times smaller to be detected.

Routine tracking of Low Earth Orbit (LEO) objects is provided to the US Space Command by the Navy Space Surveillance (NAVSPASUR) Center in Dahlgren, Va. NAVSPASUR maintains an active radar fence across the southern US which detects all non synchronous orbiting objects which cross the fence down to 10 cm in size. As the amount of space debris increases and orbiting systems become larger (Space Station) the risk of orbital collisions reaches an unacceptable level. Efforts are currently under way at NRL to actively cross correlate the current space object catalog entries with space shuttle activities in order to detect potential collisions. The orbit of the shuttle has been modified several

times in order to avoid the 10 km avoidance zone required for orbiting debris. The more precisely we know the orbital parameters of space objects the smaller the avoidance zone needs to be and the fewer shuttle (or space station) maneuvers required. The need to track all operationally critical objects requires detection of objects down to 1 cm in size. The current wavelength of the NAVSPASUR system makes detection of objects smaller than 10 cm difficult.

In order to increase the positional and velocity accuracy of space objects, additional observations are required. While visible tracking systems offer large 2 dimensional imaging capabilities, they are usually limited to 1 hour of observations before and after sunrise and sunset. The ability of visible systems to track objects depends on their reflectivity. While highly reflective objects are easily seen, dark objects are not. Thermal infrared observations appear to fill a niche allowing detection of objects smaller than 10 cm. They also offer the same positional and time resolution capabilities of visible techniques while allowing continuous observations 24 hours per day in a totally passive environment.

II Infrared Theory

In this section we will discuss the basic theory behind thermal infrared observations of space objects. Some useful formulas will be derived predicting the flux as a function of size, temperature, and emissivity. When combined with the known sensitivity of infrared detectors the integration time needed for a desired signal to noise can be calculated which in turn determines the precision with which the telescope must track the object.

II.1 Black Body Radiation

The passive thermal infrared emission from any solid object can be represented by the well know Planck formula:

$$I_\upsilon = 2\pi h\upsilon / (c^2 \ (e^{h\upsilon/kT}-1)) \qquad (1)$$

Where I_υ is the spectral radiance, h is Planck's constant, k is Boltzmann's constant, T is the temperature in degrees Kelvin, c is the speed of light, and υ is the frequency.

The above equation is modified for non black body objects by multiplying by the emissivity ε which ranges from 0 to 1 in value. Using equation (1), substituting for constants, converting to useful units, assuming a wavelength of 10 microns, and inserting source angular area in square arc seconds, we obtain:

$$F_{\upsilon 10} = \varepsilon \theta \ 2.93x10^6 \ / (e^{(1440/T)} -1) \qquad (2)$$

This equation relates the flux ($F_{\upsilon 10}$) in Janskys (10^{-26} watts/m^2/hz) at 10 microns to the angular area (θ) in square arc seconds and the temperature (T) in kelvins for a given black body with emissivity (ε). If we assume an equilibrium temperature at the Earth's distance from the Sun of 300 K°, then the equation further reduces to:

$$F_{\nu 10} = \varepsilon \theta \, 2.43 \times 10^4 \qquad (3)$$

Thus a source with an angular area of 1 square arc second which behaves like a black body would radiate 24,000 Janskys of flux at 10 microns. Note that the flux is directly proportional to the emissivity and to angular area.

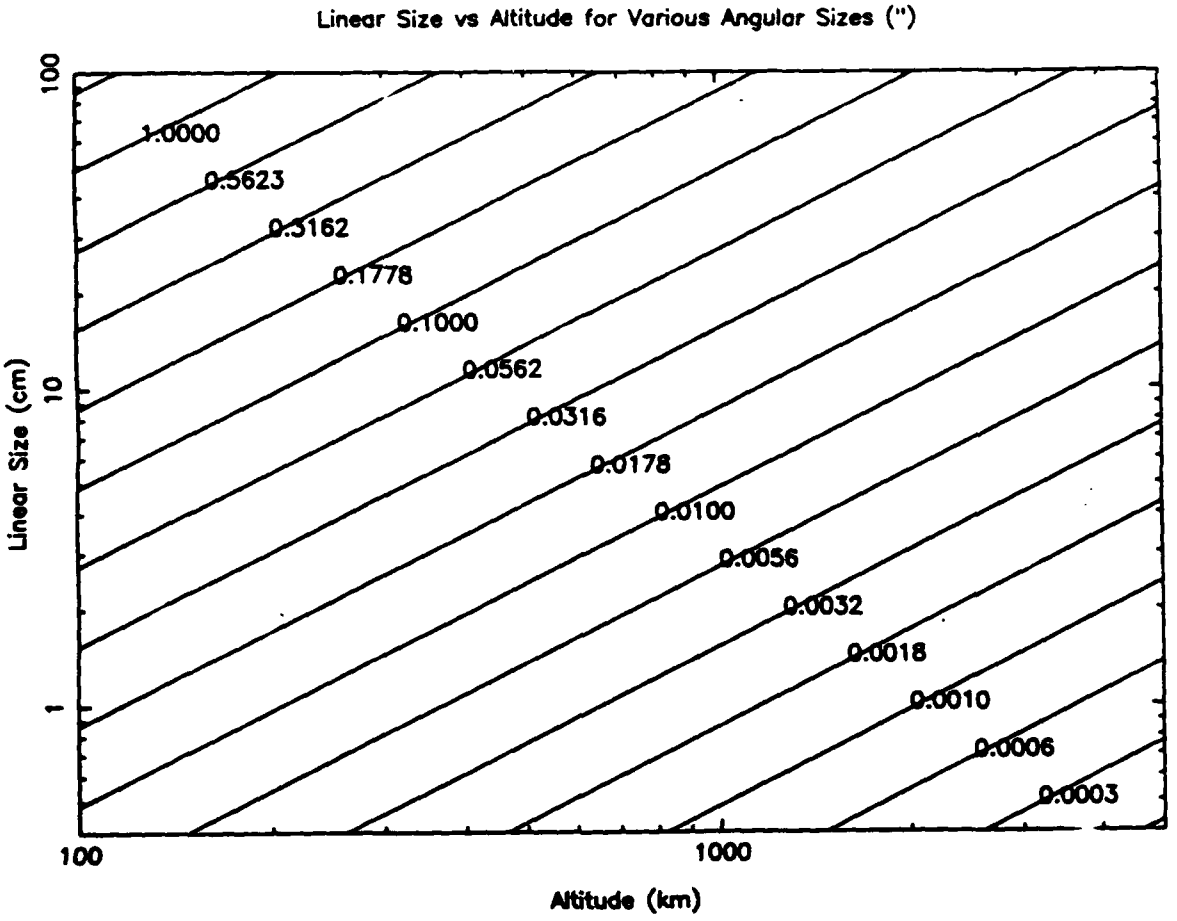

Figure 1. Plot showing relationship between linear size, altitude, and angular size.

Figure 1 is meant to be a useful plot of the linear size verses altitude for a number of different angular sizes. For example a 1 meter object subtends an angle of 1 arc second when at an altitude of 200 km. Once we know the angular size an object subtends we can calculate the infrared flux expected as a function of the emissivity.

Figure 2 shows this relationship for the two extreme ranges of the emissivity of 0.1 and 0.9. To continue our example the 1 arc second angular size would correspond to 2000 Janskys if the object had an emissivity of 0.1 and 20,000 Janskys if it had an emissivity of 0.9. These two figures can be used to quickly estimate the infrared fluxes from objects of known size and orbital altitude.

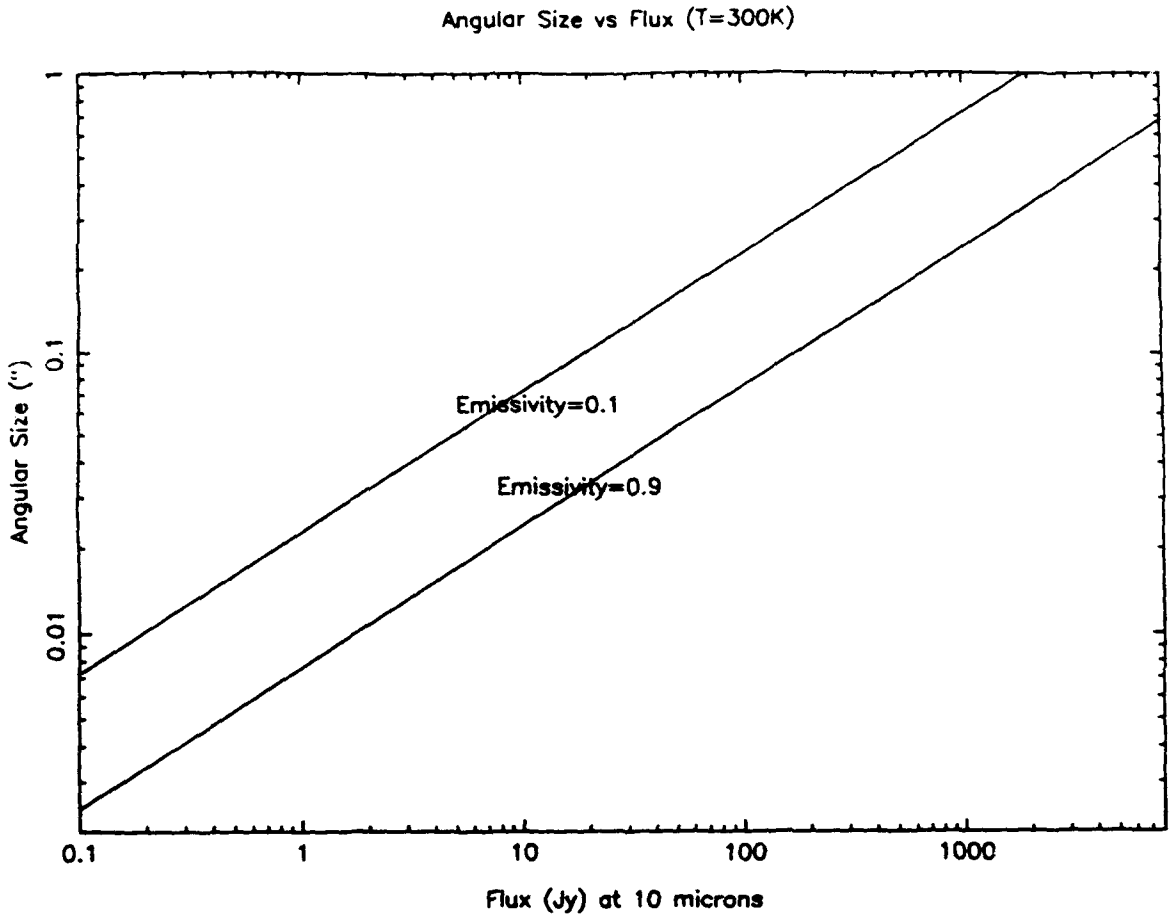

Figure 2. Plot of expected infrared flux in Janskys verses angular size.

II.2 Black Body Temperature

From equation (1) it can be seen that we have four variables: flux, temperature, emissivity and angular area. If we make measurements at two different wavelengths (10 and 20 microns in this example) and compute the ratio using equation (1) we obtain

$$F_{\upsilon 10}/F_{\upsilon 20} = (20/10)^3 * (e^{720/T} - 1)/(e^{1440/T} - 1) \qquad (4)$$

which allows us to solve for the black body temperature from only two measurements. Notice that this result is independent of source size/geometry and emissivity. Usually a simple iterative technique is sufficient to solve this equation for T.

II.3 Emissivity and Size

Now that we have an independent measurement of the temperature we return to equation (2) with two unknowns remaining, emissivity and angular size. Emissivity is limited to values between 0.1 (shinny gold) to 0.9 (black soot). The angular size of small debris objects is less than the diffraction size of modest telescopes in the thermal infrared and so cannot be directly measured. We may either assume

an emissivity and deduce a size or we could assume the Radar Cross Section (RCS) values and deduce the emissivity. The emissivity is an important physical parameter as it can easily distinguish between bright shiny mylar or a charred piece of rocket body. Emissivity enters as a linear term in equation (1) while size enters as a square. Since realistic objects will have emissivities between 0.1 and 0.9, assuming a value of 0.3 will guarantee we will be within a factor of three of the correct value. If the emissivity is off by a factor of three then the size could be off a factor of $\sqrt{3}$ or 1.7. Simply knowing the ratio of fluxes between two different thermal wavelengths will determine the true angular size within a factor of 1.7. The emissivity can be expressed as

$$\varepsilon = F_{\upsilon 10} \left(e^{1440/T} - 1 \right) / \left(2.93 \times 10^6 \theta \right) \tag{5}$$

and the angular size (D) can be expressed as

$$D = \sqrt{4\theta/\pi} = \sqrt{4/\pi \, F_{\upsilon 10} \left(e^{1440/T} - 1\right)/(\varepsilon \, 2.93 \times 10^6)} \tag{6}$$

III Observations

The infrared observations were performed with a typical astronomical telescope and infrared bolometer detector. Observations were performed at the University of Arizona's Mt. Bigelow facility housing a 1.5 m cassegrain telescope and a single channel silicon bolometer operated at solid He temperatures.

The telescope was constructed with an English fork mount and was limited from declinations North of 80 degrees. The control computer and axis drive system have recently been upgraded to allow the precision tracking needed for Low Earth Orbit (LEO) satellite observations. We did experience difficulties in tracking objects much lower than 700 km because the gear drives on the axis would begin to bounce and accurate tracking became difficult. Future tuning of the drive feedback parameters may relax this restriction on subsequent runs. Satellite tracks which approached the zenith were chosen to increase the track time as much as possible. Unfortunately, moving the dome to keep up with the track was a significant problem near the zenith. Clearly, using a telescope with a drive system and dome designed for LEO tracking in the beginning would be preferred.

The detector is a vintage silicon bolometer housed in a dewar and operating at solid He temperatures (~1.2k). The bolometer contained a number of infrared filters including standard ones at 10 and 20 microns, but they required manual selection which prevented us from getting measurements at both wavelengths for the lowest satellites. The system contained an intensified guider eyepiece which was used to acquire the satellites since it was too hard to track with a single channel detector. If the sensor had been a two dimensional infrared focal plane array then acquiring the satellite in the visible would not have been required and 24 hour per day observations could have been performed.

Standard stars were observed throughout the night whenever there was a break in the schedule. Observations were then corrected for airmass effects and converted to absolute flux measurements following standard astronomical techniques.

Current orbital elements could be acquired either directly from NAVSPASUR using a modem or over

the internet using the NRL Connection machine which calculates current element sets and propagates them forward looking for orbital collisions.

IV Results

Table 1 shows the observational results obtained on November 4-6, 1993. The satellite numbers conform to the US Space Command's numbers where "a" and "b" represent data sets from different nights, RCS is the accepted average radar cross section in square meters, Dist is the mean value of the satellite altitude at time of observation in km, Band1 represents the 10 micron flux measurements expressed in Janskys, Band 2 same as Band 1 but for 20 microns, Size is the projected RCS at DIST in arc seconds, IRSIZE is the radiometric black body size determined from equation (6) assuming emissivity of 0.3 also expressed in arc seconds, EMISS is the infrared emissivity determined from equation (5) assuming RCS is correct, and IRTEMP is the infrared black body temperature determined by using equation (4) expressed in degrees Kelvin, * indicates a temperature of 300K° was used for the other calculations.

SAT #	RCS (m^2)	DIST (km)	BAND1 (10μ)	BAND2 (20μ)	SIZE (")	IRSIZE (")	EMISS	IRTEMP (K°)
22178a	5.0	30500	8.2	7.2	.017	.021	0.46	395
22178b	5.0	22500	18.0	24.0	.023	.051	1.45	313
20302a	1.8	21200	3.4	3.3	.015	.015	0.31	372
20302b	1.8	21500	0.8	-	.015	.012	0.19	*
21227a	25.7	37000	3.0	3.5	.032	.018	0.09	335
21227b	25.7	37000	3.9	3.6	.032	.015	0.07	383
21392a	4.5	37600	2.5	2.3	.013	.012	0.27	384
21392b	4.5	37600	2.0	-	.013	.019	0.62	*
1642	4.2	770	600.0	-	.620	.320	0.08	*
20255	0.8	14800	25.0	25.0	.014	.043	2.80	365
7095	5.9	1200	530.0	-	.470	.310	0.16	*
15271	0.2	22700	2.9	4.9	.005	.026	7.90	284
1314	11.2	1500	400.0	-	.520	.270	0.08	*

Table 1. Summary of Observations and Results

If we take into consideration the fact that we are comparing averaged quantities and that the RCS and infrared measurements were not carried out simultaneously then the results appear self consistent except for two objects, satellite numbers 20255 and 15271 which show calculated emissivities much larger than 1 which is inconsistent with black body radiation. Since some of the satellites are active, a detailed thermal model would be needed to fully understand what the IR measurements represent.

If we assume we have a modern 2 dimensional focal plane array and ask what size of objects can we detect using the above equations we produce a graph represented as figure 3. The three main quantities which determine the sensitivity are angular size of the object, sensitivity of the infrared detector, and the integration time we can expect for a given pixel which is determined by the ability

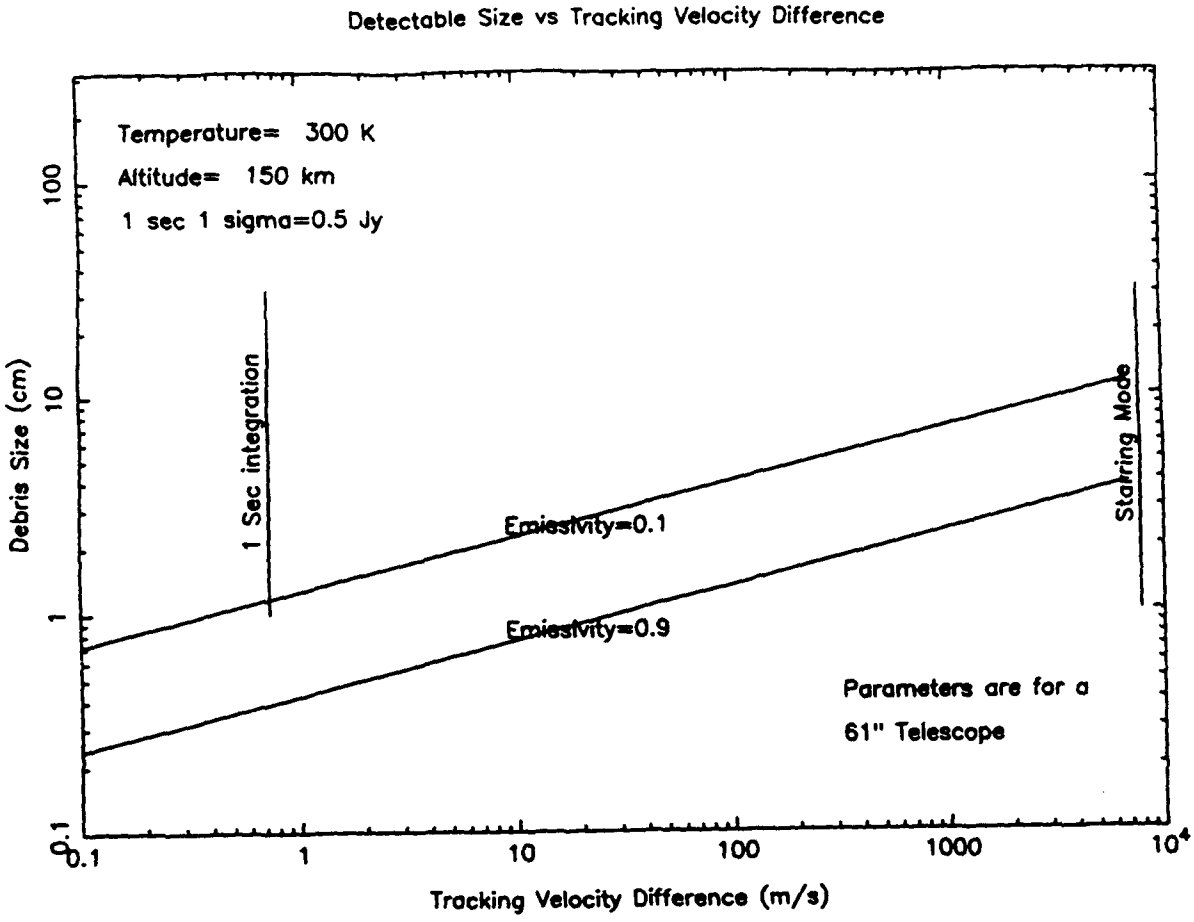

Figure 3. Detectable size limits as a function of velocity knowledge and emissivity.

to track an object and keep it on a detector element. A pixel size of 1 arc second was assumed. The tracking velocity difference represents our ability to know or track with the same velocity as the satellite. This determines how long an integration occurs at a particular pixel.

The short vertical line labeled "1 sec integration" show the sensitivity obtained in 1 second of time. It is also positioned over the velocity difference needed to produce this integration. The short vertical line labeled "starring mode" represents the sensitivity achieved when the sensor is starring and has no velocity information about the object. The horizontal axes is the tracking velocity difference between the telescope and the object. If we have no velocity information about the satellite then a detector with a 1 arc second pixel size will only get to integrate for 0.0001 seconds. The 1 second 1 sigma sensitivity limit for a good modern infrared detector at 10 microns is 0.5 Jy (for this size telescope). This implies we need about a 500 Jy source for a 1 sigma detection in surveillance mode. Using figure 2 we find that we need a angular source size of 0.2 arc seconds. At 150 km altitude this corresponds to a source size of 10 cm. As our ability to track an object and match the velocity increases the source detection size decreases. If we can keep the object on a single pixel for 1 second we could observe objects down to less than 1 cm in size. Keep in mind that these sensitivities are appropriate for excellent astronomical observing conditions and will degrade in the

presence of high humidity, thin cirrus clouds and other non-photometric conditions.

III Future Improvements

The limits given above for detection when no velocity information is known (surveillance mode) could be reduced further with the use of modern digital image processing. If we obtained a frame from a 256 x 256 pixel detector and simply do coherent additions for different tracks across the array, we could reduce our limiting size by almost an order of magnitude. An order of magnitude would require the coherent addition of a track over 100 pixels long. The finest rotational unit over the 50 pixel extent is of order 1 degree. Thus we need to add about 100 pixels 180 times to cover the area centered around one point. This corresponds to 100x180 or 18,000 additions. IR focal plane arrays of the considered size are read out near 200 hz frame rates giving 3.6 MFLOPS per pixel in the array. A 100 x 100 region of the array would require 36 GFLOPS of processing power. This is an overestimate since we did not take redundant operations of overlapping regions into account. This is near the processing power of the NRL connection machine. If the sensor were connected to the connection machine by fiber optics running an ATM network, then real time processing of the array would extend the surveillance detection limit below 1 cm in size.

These observations were carried out with a modified astronomical telescope using a single channel bolometer detector. The quality of the data is testimony to the diligent observing capabilities of the Steward observatory astronomers. The next step would be to construct a modern two dimensional imaging infrared focal plane camera and finally design a dedicated telescope which could routinely observe cm sized LEO objects and update US Space Command catalogs in real time 24 hours per day.

IV Acknowledgments

Special thanks to the following NAVSPASUR people who provided accurate orbital elements which were required for this project: Neil Melson, Jon Boers, and Terri Smith. Thanks to the NRL space collision project for also providing updated elements and predictions: Shannon Coffey and Bernie Kelm. Thanks to the Steward Observatory astronomers whose diligent observational expertise made these observations possible: George Rieke and Marcia Rieke.

Detection of Centimeter Sized Space Debris

J.J. Atkinson, G.E. Galica, S.A. Rappaport, O. Shepherd, R.A. Skrivanek (Visidyne, Inc.),
W.S. Borer (Phillips Laboratory/Geophysics)

Abstract

A vexing problem to anyone attempting to specify the space debris environment in near earth space has been the paucity of measurements of debris pieces in the 0.1 to 10 centimeter size range. Recent LDEF measurements of micron-sized particles and ground based optical and radar measurements of debris larger than 10 centimeters, more recently as small as 0.4 centimeters, do not completely fill this critical gap, especially for nonconducting debris. As part of a Small Business Innovative Research effort, a small optical space debris detector suitable for satellites and capable of measuring the size and flux of debris in this critical size range has been designed and is now being fabricated. This instrument uses a passive charge-coupled detector mated to wide-angle optics to continuously view a large conical volume of space in the vicinity of the orbiting spacecraft. When a debris particle passes through the field of view, sunlight is scattered into the telescope and is sensed by the CCD. The resultant information is analyzed with an innovative on-board signal processor. Frames that contain debris tracks are then telemetered down for further analysis. Based on the NASA Space Debris Model, calculations show that this instrument will detect hundreds of particles per year in the size range of interest. This paper is unclassified.

Introduction

Since 1957, when the first man-made satellite was launched into earth orbit, more than 3400 launches have created a population of some 7000 trackable objects (that is, objects larger than about 10 cm) in near-earth space. Only about 400 of these objects are active spacecraft; the remainder are space debris, objects which are threats to all present and future spacecraft. Of the 7000 trackable objects, about half are fragments resulting from explosions or breakup of satellites and rocket bodies. In addition to the large trackable fragments that result from these events, there are also a much greater number of smaller objects, with sizes ranging from a few centimeters down to a few microns, that cannot be detected or tracked from the ground.

Detecting particles or fragments in this size range has presented researchers with formidable problems. A major advance was recently made when the LDEF space platform was recovered from space after a 68 month exposure to space debris. The various experiments on that platform yielded excellent statistics on the flux of debris particles in the size range of one to several hundred microns. Unfortunately, the particle population in the millimeter to centimeter size range was not measurable with the LDEF concept, and hence the flux of these particles remains unmeasured and subject to large uncertainties. This lack of reliable data for debris particles in the millimeter/centimeter size range presents a problem to spacecraft designers because these particles travel at very high velocities and can inflict major (perhaps even catastrophic) damage on an orbiting spacecraft. The larger (>10 cm) particles, being detectable and trackable by radar, can be avoided by a slight adjustment to a spacecrafts orbit; the effects of collisions by smaller particles (<1 mm) can be negated by the use of meteor bumpers covering the critical parts of a spacecraft, without incurring too large a price in terms of added weight.

Millimeter/ centimeter size particles, however, are too small to be seen with radar and are sufficiently large to make shielding impractical. In the future, our space program, with its aggressive plans for larger, longer lived, spacecraft, will require an accurate description of the space debris particle population in this range of sizes in order to assure space operations with acceptable levels of risk.

Detection of orbital debris from the ground has consisted primarily of observations made by the radars of the Space Surveillance Network (SSN). The network's limiting sensitivity of around ten centimeters has prompted several campaigns using the shorter wavelength radars at Goldstone, Arecibo, and most recently Haystack. These radars have succeeded at measuring objects as small as five millimeters, but have not been able to establish tracks and orbital elements for the detected objects.

Earth based telescopes operating in the visible part of the spectrum, have augmented the radar data base. NASA has used a portable telescope as well as the Ground Based Electro Optical Deep Space Surveillance (GEODSS) assets at Diego Garcia to observe debris in low earth orbit. Recently, the Lincoln Laboratory Experimental Test System and the AF Space Command's AMOS observation teams have perfected detect and track capability for optical observations of objects in low earth orbit. These improved capabilities have resulted in the establishment of reliable orbital elements for the detected objects. The sensitivity of these ground based optical sensors, however, is about the same as those of the SSN, with the exception that the optical techniques are sensitive to nonconducting debris. The sensor described in this paper will complement the aforementioned observations by detecting objects much smaller than ten centimeters using the same principle of visible solar scattering.

One important conclusion from the earth-based observation campaigns is that the optically reflecting population is very different from the radar-credible population. That is, radar-credible targets are often not seen with optical telescopes and optically bright objects often go undetected by ground based radars. So far, no confirmation of this non-overlap has been established for the smaller than ten centimeter population. Accurate population counts of the less than ten centimeter population with this optical sensor will be able to answer this question through comparison with the earth based radar observations of the corresponding radar-credible population.

Recognizing the situation described above, the Phillips Lab/Hanscom requested the Small Business Innovative Research Program to solicit for an innovative method of measuring the flux of space debris particles in the critical mm/cm size range. Satellite measurements have been seen as a fruitful direction in which to proceed; however, the known methods for carrying out such measurements have heretofore been generally limited to the detection of very small particles, as in the case of LDEF. In order to observe a useful number of millimeter/centimeter sized particles per unit time, a very large area of space must be monitored, and small signals from very fast moving particles will have to be detected and recorded. Visidyne's proposed proprietary design to extend satellite measurements to mm/cm scale particles was selected by Phillips Lab, and a subsequent Phase I study was performed. That study has produced a design for an instrument that is fully capable of making statistically meaningful measurements of the flux, size, and velocity of debris particles in this size range.

During the Phase I effort, Visidyne developed several innovative and proprietary approaches in electro-optical design that now permit the detection and measurement of millimeter/centimeter sized debris particles. One of these innovations is the concept of stepping a charge coupled device while it is viewing a hypervelocity debris particle as a means of applying temporal marks to the debris track in the image. With these temporal marks, angular velocity of the particle can be measured and range from the camera to the particle can be inferred, a necessary parameter for determining its size. It is upon this technique that the Space Particle Imager (SPI) discussed herein is based.

The approach developed by Visidyne uses a passive charged-coupled detector mated to a wide-angle telescope that continuously views a large conical volume of space in the vicinity of the orbiting spacecraft. When a debris particle passes through the field of view, sunlight is scattered into the telescope and sensed with the CCD. Because of the high velocity of the debris particles relative to the spacecraft, they will typically traverse the field of view of the camera in less than one frame integration time. The CCD therefore records the particle as a streak in the image rather than a single point. The resultant information is passed on to a microcomputer signal processor, which examines the image frame and tests for the presence of a particle track. If a particle track is found, the image data are stored until they can be telemetered to the ground. Otherwise, the data are discarded. This onboard selection greatly reduces the burden of the instrument on spacecraft telemetry resources. Image data, complete with temporal marks on the particle track, are analyzed on the ground to determine particle trajectory, range, and size.

The SPI Camera

According to the NASA standard debris model, the population of particles in the size range of interest is relatively small. Therefore, a large volume must be searched to obtain a statically significant number of detections. A primary requirement for the SPI camera is, therefore, that it view the largest possible volume of space. To accomplish this a TK1024AB CCD from Scientific Imaging Technologies (SITe, formerly Tektronix) was chosen. It is a 1024 x 1024 array with large, 24 x 24 micrometer pixels for a total sensitive area of 24.6 mm square. In addition, the TK1024AB is back illuminated for high quantum efficiency and can be operated in MPP mode for low dark current and low noise, both of which improve the signal to noise ratio. Coupled with a 50 mm focal length f/1 lens, the camera has a field of view of about 28 x 28 degrees. The other parameter that determines the size of the sampled volume for a given particle size is the maximum range at which particles can be imaged with sufficient signal to noise to be detected. The noise is comprised of the RMS sum of three terms: (1) the shot noise due to the celestial background, (2) shot noise due to CCD dark current, and (3) CCD amplifier and readout noise. The design goal was to build a detection system with a low detector noise contribution so that the noise is dominated by the celestial background.

The signal per pixel per frame, S, produced by the solar scattering from a moving debris particle is given by

$$S = \int_{\lambda_1}^{\lambda_2} f_{sun} \frac{d\sigma}{d\Omega} \frac{A}{R^2} \eta \; T \; t \; d\lambda \qquad \text{(counts pixel}^{-1}\text{ frame}^{-1}\text{)} \qquad (1)$$

where f_{sun} is the solar spectral irradiance, expressed in photons cm^{-2} sec^{-1} nm^{-1}, $d\sigma/d\Omega$ is the partial differential scattering cross section expressed in cm^2 sr^{-1}, A is the area of the collection optics (cm^2), R is the range to the particle (cm), η is the quantum efficiency of the detector, T is the transmission of the optics, and t is the length of time that the particle resides in a particular pixel. The integral is performed over the visible wavelength region (300-900 nm). The scattering cross-section, for a scattering angle of 180°, is given by [1]

$$\frac{d\sigma}{d\Omega} = \frac{2}{3\pi} \alpha \; \pi r^2 \qquad (cm^2\ sr^{-1}) \qquad (2)$$

where α is the albedo of the particle and r is its radius. The pixel residence time, t, for a particle moving through the field-of-view of the sensor is given by

$$t_{resid} = \frac{\theta_{pix} R}{v} \qquad \text{(sec)} \qquad (3)$$

where θ_{pix} is the pixel field of view, R is the particle range, and v is the particle velocity. The upper bound on t_{resid} is the overall integration time per frame; i. e., particles at very long ranges will remain in a single pixel for an entire integration time (4 sec). At these very long ranges, particles large enough to be detectable are larger than the maximum size of interest. The particle detection algorithm employed by the signal processor will be insensitive to those particles and they will not be detected.

There are several sources of noise in this measurement: detector dark noise, amplifier and readout noise, and the fluctuations in the celestial background. The typical dark current for the TK1024AB, a back-illuminated array with MPP operation is 0.1 nA cm^{-2} at 20° C. This dark current typical doubles every 5-7° C. The dark signal per pixel is then given by

$$B_{dark} = \frac{1}{q} J_{20} \, 2^{(T-20)/6} \, A_{pix} \, t_{int} \qquad \text{(counts pixel}^{-1}\text{ frame}^{-1}\text{)} \qquad (4)$$

where q is the charge on the electron, J_{20} is the dark current per unit area at 20° C, T is the array temperature in °C, A_{pix} is the area of the pixel (24 μm × 24 μm), and t_{int} is the integration time. The dark noise then is given by

$$N_{dark} = \sqrt{B_{dark}} \qquad \text{rms counts pixel}^{-1} \qquad (5)$$

The dark noise is evaluated in Table 1.

Table 1
Dark Signal and Dark Noise for the SPI Detector Array [U]

temperature (°C)	dark signal, B_{dark} (counts pixel^{-1} frame^{-1})	dark noise, N_{dark} (rms counts pixel^{-1})
20	14,400	120
0	1430	38
-20	142	12

The on-chip amplifier noise per pixel is specified as 7-10 rms electrons at -90° C for a readout rate of 50 KHz. SITe provides a temperature scaling curve for the amplifier noise. In addition, since this device will operate at 750 KHz, which is within the maximum operating rate, we have scaled the noise by the square root of the ratios of the frequencies. The amplifier noise, N_{amp}, for this sensor then is given by

$$N_{amp} = N_{(-90,50)} \frac{N(T)}{N(-90)} \left[\frac{f}{50}\right]^{1/2} \quad (6)$$

where $N_{(-90,50)}$ is the amplifier noise at -90° C and 50 KHz and f is the readout rate for the SPI sensor (750 KHz). The amplifier noise is evaluated in Table 2.

Table 2
Amplifier Noise for the SPI Detector Array [U]

temperature (° C)	N(T)/N(-90)	N_{amp} (T, 750 KHz) (rms counts pixel^{-1})
20	4.8	130-185
0	2.4	65-93
-20	1.5	41-59

The average radiance from the celestial background near the galactic plane, L_{celest}, is 9.1×10^{-18} W cm^{-2} deg^{-2} Å^{-1}. The signal from the celestial radiance is given by

$$B_{celest} = L_{celest} \frac{\Delta\lambda}{h\nu} A\ \Omega\ \eta\ T\ t_{int} \quad (7)$$

$$= 6920 \quad \text{counts pixel}^{-1}\ \text{frame}^{-1}$$

where $\Delta\lambda$ is the spectral bandpass of the sensor (300-900 nm), hν is the photon energy, A is the area of the collection optics (20 cm^2), η is the quantum efficiency of the detector (0.8), T is the

transmission of the optics (0.9), and t_{int} is the integration time (4 sec). The noise due to the fluctuations in the celestial background, N_{celest}, is given simply by the square root of the actual background signal and is equal to 83 rms counts pixel^{-1}. The total noise is obtained by summing the noise terms in quadrature. The three noise terms and the total noise are evaluated in Table 3.

Table 3
Noise Contributions and Total Noise for the SPI Sensor [U]

T (° C)	N_{amp}	N_{dark}	N_{celest}	N_{total}
20	130	120	83	195
0	65	38	83	112
-20	41	12	83	93

For temperatures above 20° C, the dark noise and amplifier noise dominate. For operational temperatures below 0° C, the dominant noise term is the noise in the celestial background; therefore, our goal is to operate the SPI focal plane at or below 0° C.

The actual celestial background consists of many dim stars that form a pseudo-continuum background, and comparatively few bright stars that appear as discrete sources. In that sense, this treatment of the celestial background is inexact, but still serves as a useful approximation for the sensitivity calculations. We have performed a full sensor simulation taking into account the cluttered celestial background, the MTF of the optical system, the apparent motion of the debris particles, the SPI time tagging, and the other sensor noise terms. The results of the full simulation are consistent with these estimates of sensor sensitivity.

The signal-to-noise ratio is given by

$$SNR = \frac{S}{N_{total}} \tag{8}$$

After rearranging the expression for the scattering signal, we find that the minimum detectable particle size, r_{min}, is given by

$$r_{min} = \left[\frac{3 \cdot SNR \cdot R \cdot v \cdot N_{total}}{2 \cdot \alpha \cdot A \cdot \theta_{pix} \cdot \int_{\lambda_1}^{\lambda_2} f_{sun}\, \eta\, d\lambda} \right]^{1/2} \quad \text{(cm)} \tag{9}$$

The above equation holds as long as t_{resid}, given by equation (3), is less than the four second integration time.

We have evaluated this expression as a function of range, assuming a detector temperature

of 0° C, and a relative linear velocity of 10 km/sec for a signal-to-noise ratio of three. The results of that evaluation are given in Table 4.

Table 4
Minimum Detectable Particle Size (SNR=3) as a Function of Range
for the SPI Sensor [U]

Range	r_{min} (cm)
100 m	0.18
300 m	0.31
1 km	0.57
3 km	1.0
10 km	1.8
30 km	3.1
100 km	5.7
300 km	10

The results summarized in this table demonstrate that the SPI will have the capability to augment the existing database of space debris measurements in the critical 0.1 to 10 cm range. Estimated detection rates are calculated, based on the NASA model at an altitude of 500 km, to be 25 particles per day for particles less than 10 centimeters and 100 particles per year for particles less than 1 centimeter in diameter.

The TK1024AB is a full frame imager, and so a shutter is required to prevent smearing of the image during readout. Operated at its specified maximum rate, a frame can be read out of the TK1024AB in about 1.6 seconds. An integration time of four seconds yields an operating duty cycle of about 70% with acceptable signal to noise performance at 0°C.

Measurement Technique: Time Tagging the Particle Tracks

The basic measurement concept is quite simple. The camera is to be mounted on board a spacecraft in a circular, sun synchronous, dawn to dusk orbit, and oriented so that it is looking in the tangent plane and away from the sun. In this way, the sensor views solar illuminated particles against a dark celestial background, which is necessary for the detection of the scattered light signals from small particles. This orientation also provides scattering angles close to 180 degrees, which enhances the detected signal (for nonforward scattering geometries). Particles cannot be detected against hard earth or limb backgrounds, or when the spacecraft is in the earth's shadow. The sun synchronous dawn to dusk orbit maximizes the amount of time spent in the optimal viewing geometry. The size of the particles can be calculated from the scattered sunlight signal measured by the detector if the range from the particle to the detector, its albedo, are known.

Determining range is the first part of the problem. Given the assumption that the detected debris particle is in a circular orbit of about the same altitude as the sensor, its relative linear velocity can be inferred. The angular velocity is measured by the sensor, and the range can then be calculated from the inferred value of particle linear velocity. One approach might be to utilize a detector capable of very high frame rates so that a particle might be captured in two or more successive frames. Since the angular extent of each pixel is a known function of the pixel size and the optics, the angular velocity would be determined by measuring the number of pixels traversed in one frame time. The difficulty with this scheme is that for smaller particles, which will only be detectable at relatively close range, the time to traverse the frame is very short. For example, array transit time is on the order of 5 milliseconds for: range=100m, v=10km/sec, and FOV=30°. Large (1K x 1K pixels) commercially available CCD focal plane arrays with large pixels, which are required to attain the large field of view, however, are incapable of frame rates beyond a few hertz.

The SPI employs a new technique for determining the angular velocity of a particle traversing its field of view in less than one frame time. This allows the use of available CCDs at low frame rates (4 seconds/frame). During integration of the scene, the charge accumulated in the CCD wells is shifted up and down at short intervals, in this case every 4 milliseconds. Due to this shifting, a straight line track across the field of view is recorded in the image as a stepped line with a vertical jog every 4 milliseconds. Angular velocity is easily determined by counting the number of pixels that the particle has traversed between two marks. An idealized frame with a time tagged particle track is shown in Fig. 1. For particles whose transit times are much greater than four milliseconds, several marks will be present on the track allowing multiple independent measurements of the particle's angular velocity. Also, particles that cross the field of view at other than a right angle to the camera's optical axis (i.e. moving towards or away from the camera) will produce an apparent acceleration. The closer the particle gets to the camera, the longer each 4 millisecond segment will be. By measuring this apparent acceleration, the particle's trajectory can be determined. For particles at very close range where only one temporal mark may be present, as is the case for particles at 100 meters, angular velocity can still be determined. The vertical jogs are not instantaneous (a step of four lines takes about one millisecond); therefore, velocity can be determined from a single temporal mark by measuring the difference in slope between the segment that was recorded during the step and that recorded during the dwell period between steps.

Figure 2 shows a simulated scene with a time-tagged particle track. The simulation includes the effects of CCD noise, noise due to the celestial background, clutter from discrete stars in the background and the MTF of the optics. The step size for the temporal mark is four lines per step. The temporal marks are difficult to discern in Fig. 2, but become clearly apparent in Fig. 3, which is a magnified view of the same image.

Camera Mechanical and Thermal Design

Figure 4 shows the mechanical layout of the camera. The requirement that the CCD be maintained below 0°C is the principle driver for the thermal design. It was decided to use passive thermal control rather than an active cooler such as a peltier device to maintain the CCD temperature. The passive approach is inherently more reliable and more efficient in terms of power consumption and weight. Since only the CCD needs to be cooled, the camera is divided

into a "cold" side and a "hot" side. The hot side consists of the baseplate and bulk of the electronics, which are mounted to it. The electronics conduct their heat into the spacecraft structure via the baseplate and do not load the radiator. The cold side consists of the top surface, which is the thermal radiator and lens mount, and a rectangular dish suspended from it. It is held off the baseplate by a fiberglass epoxy truss and so is well isolated from the spacecraft. The CCD and supporting circuitry are housed in the rectangular dish that is suspended from the radiator. Thus the thermal load on the radiator is kept to a minimum and only those components that need cooling are connected to it. With the surface area provided, the radiator is capable of rejecting about 7 watts at a temperature of 250 K. The estimated power dissipated by circuitry in the dish is about 1.5 watts. The remaining margin will be sufficient to maintain the CCD temperature in spite of thermal leakage through the fiberglass epoxy structure and wiring. To minimize thermal radiation from the hot side to the cold side, multi-layer insulation (MLI) will be used.

Camera Electronics Design

The block diagram in Fig. 5 shows the electronics necessary to operate the CCD. The preamplifier and clock drivers are located in the cold section of the camera near the CCD for optimal noise performance. The rest of the electronics are located on the hot side. To simplify the interface between the camera and the signal processor and to minimize the potential for noise pickup in the video signal, the video data are digitized in the camera. Resolution of the video data is 12 bits. A correlated double sampling circuit removes the CCD reset noise prior to digitization.

Radiation tolerance is a concern in choosing electronic parts. In the case of the CCD, however, performance over the life of the mission cannot be guaranteed by parts selection alone. Fortunately, degradation of the CCD with radiation dose tends to be a gradual process, and its effects can be compensated for to some extent by adjusting the bias and clock voltages. For this reason, the SPI camera incorporates a bias voltage regulator that is fully programmable in flight. Both clock high and low voltages, and dc biases, are set by digital to analog converters (DACs). The DACs are loaded with default values on power up by the microcontroller in the signal processor. Should adjustment be required, alternate DAC data can be uplinked.

Other functions include a motor and motor driver for the shutter, an in flight test lamp, a timing generator to control the CCD clocking, and housekeeping monitors for various voltages, currents, and temperatures. The camera has no direct electrical interface with the spacecraft; it receives its power and commands from the SPI signal processor and returns digital video and housekeeping data. Two separate data interfaces are used. Video data is transmitted over a dedicated unidirectional high speed digital link. Housekeeping and command data are transmitted and received over a low speed general purpose serial interface. Power converters to provide all of the necessary voltages to operate the camera are located in the signal processor. This keeps the potentially noisy power converters far removed from the sensitive low level CCD output.

Signal Processor

The image data from the camera contains all that is necessary to detect and measure particles. In theory, every image frame could be telemetered to the ground for processing, thus eliminating the need for an onboard processor. However, with one frame produced every 5.6

seconds, the average data rate would be about 2.25×10^6 bits/second, exclusive of any housekeeping data that may be required. Storage and transmission of this much data would place a severe burden on the spacecraft telemetry resources. It is also quite wasteful; as stated previously, the anticipated detection rate is only 25 particles per day. If only those frames that contain a particle track are telemetered, the estimated average bit rate drops to about 3600 bits/second. The economy of employing an onboard signal processor is readily apparent.

The algorithm employs a Hough transform to test for the presence of a track in the image. Note that all processing steps are performed nondestructively, so that the original image with full resolution is retained in memory throughout. First, the 1024x1024 pixel image is re-binned to form a 256x256 image by summing the signal from each 4x4 segment of the original image into one pixel in the new image. This accomplishes two things. First, it reduces the number of computational steps that will be required by reducing the total number of pixels. Second, it enhances the ability of the Hough transform to find tracks that have been time tagged. One side effect of the time tagging technique is that is takes the "lit" pixels due to a single particle track and spreads them out into two collinear sets of points. Since the Hough transform is geared to search for collinear points, the time tagging has the effect of obscuring the track slightly. While this effect is negligible for cases where signal to noise and signal to clutter are high, we cannot tolerate losing low signal to noise scenes because they are likely to have the most interesting data, i.e. small particles. Because the time tag step size is 4 pixels, rebinning on a 4x4 basis effectively puts all of the lit pixels back along a single straight line where they have the best chance of being detected by the Hough transform.

Once the image is rebinned at the lower resolution, it is thresholded to produce a binary image. The Hough transform operates on the 256x256 binary image and produces a corresponding image in Hough space. A differencing filter is then applied to the Hough image to remove artifacts produced by a cluttered background in the original image, and the result is thresholded to test for peaks above a preset limit. A peak in the Hough transform corresponds to a potential track in the image. The presence of a peak exceeding a controllable threshold means that there is a potential track in the original 1024 x 1024 data and that image frame is telemetered to the ground station.

To perform the above algorithm in real time, it is calculated that the signal processor must perform approximately 10.7 MFLOPs per second. This level of performance is consistent with that obtainable from currently available digital signal processor (DSP) chips. Other features of the signal processor can be seen in the block diagram in figure 5. In addition to the DSP, a general purpose processor is used to perform housekeeping tasks and to service the spacecraft data and command interfaces. Power converters are housed in the same package with appropriate filtering and shielding to prevent electromagnetic interference from radiating or from being conducted out onto the interconnect cables.

Conclusion

In light of the importance of the space debris problem, an effort to improve the knowledge base in this area is appropriate. The Space Particle Imager, SPI, can make a significant improvement in that base by providing high quality data on the flux and trajectories of particles between 0.1 centimeters and 10 centimeters where data are most scarce.

References

[1] van de Hulst, H.C., "Light Scattering by Small Particles", (Dover, New York, 1981).

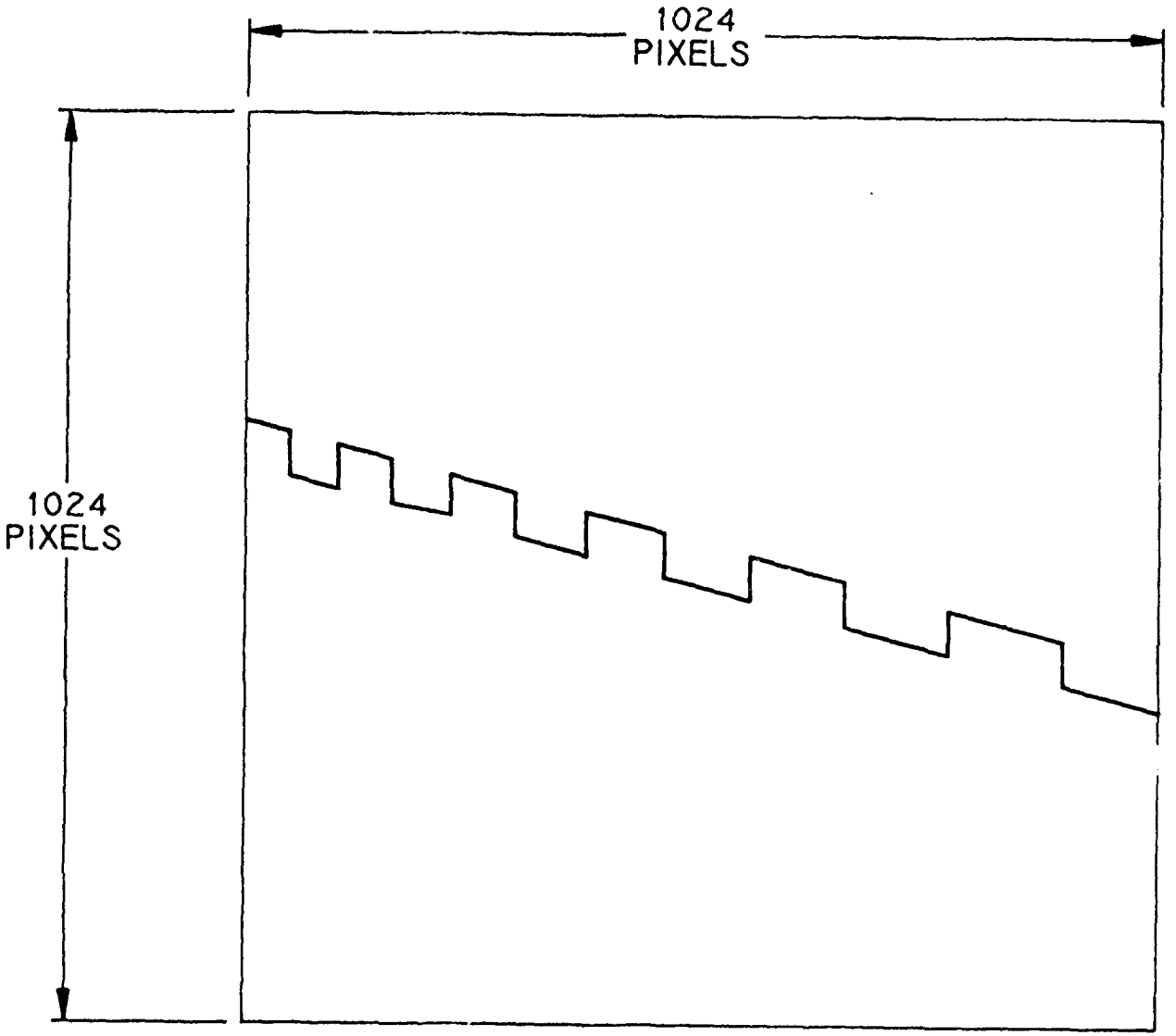

Figure 1

Sketch of a particle track across the field of view of the SPI detector, with temporal marking.

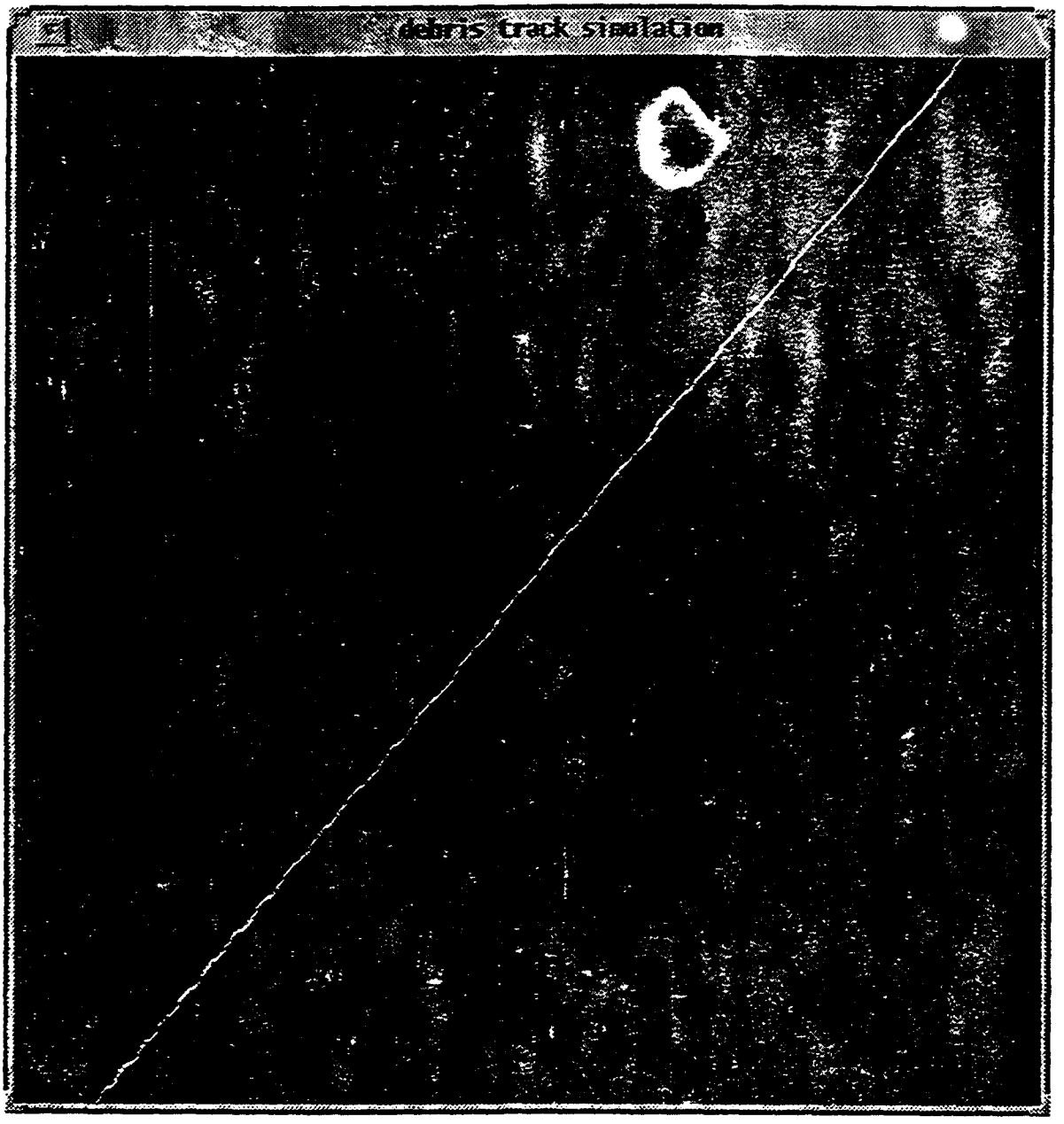

Figure 2

A simulated scene with a debris track with temporal marks against a realistic background

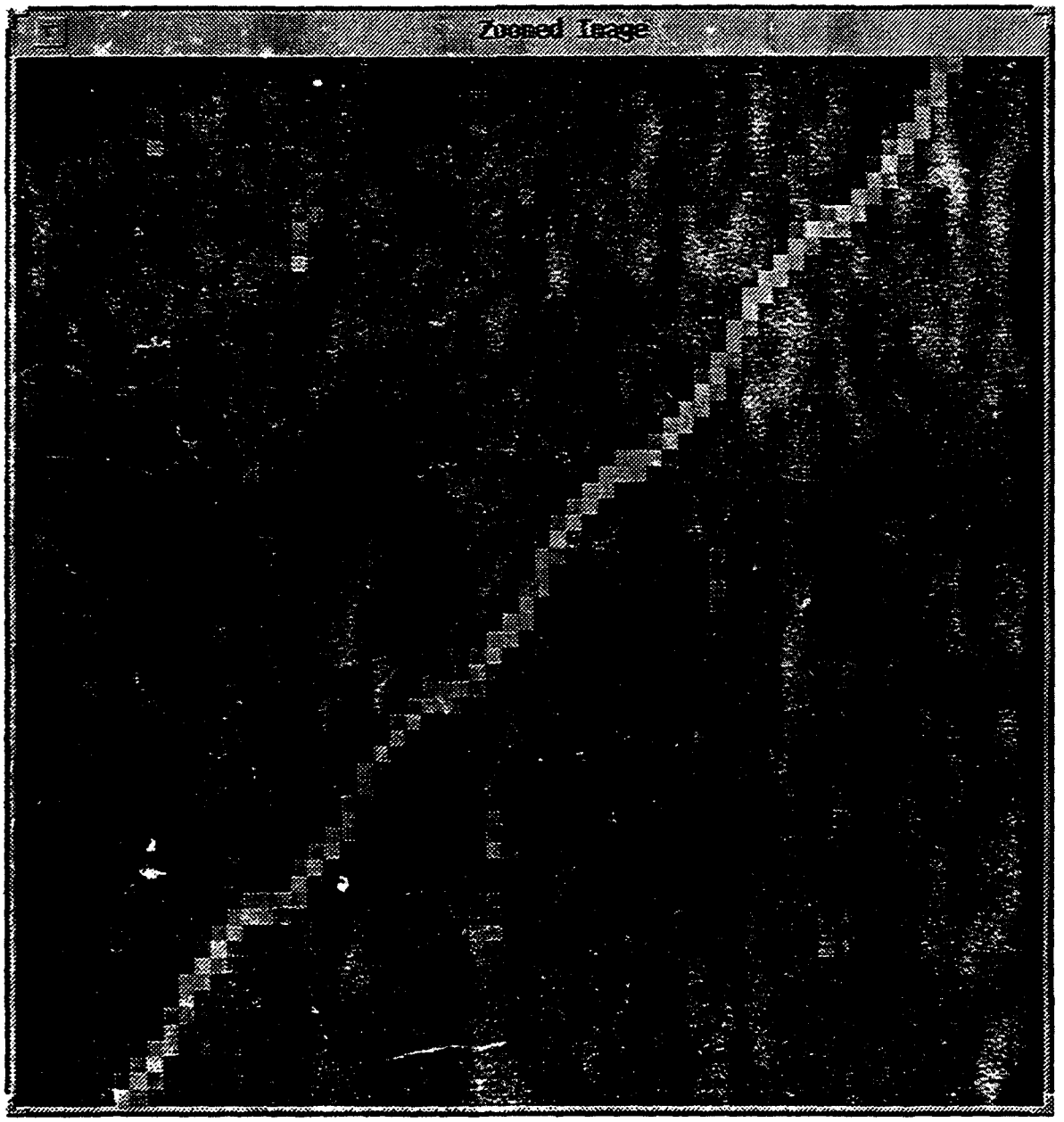

Figure 3

An expanded view of the simulated scene shown in Fig. 2

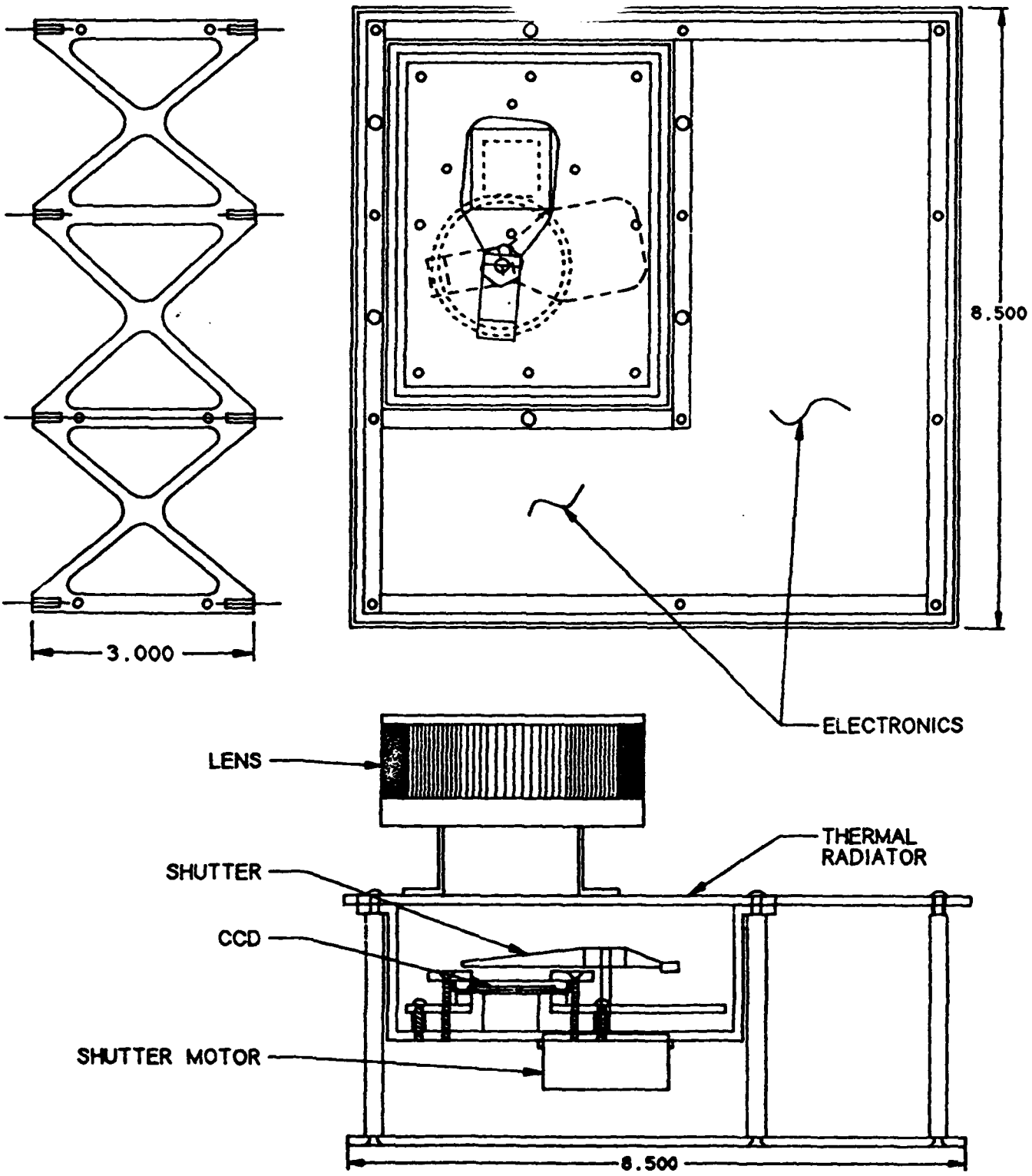

Figure 4

Physical Layout of the SPI Camera

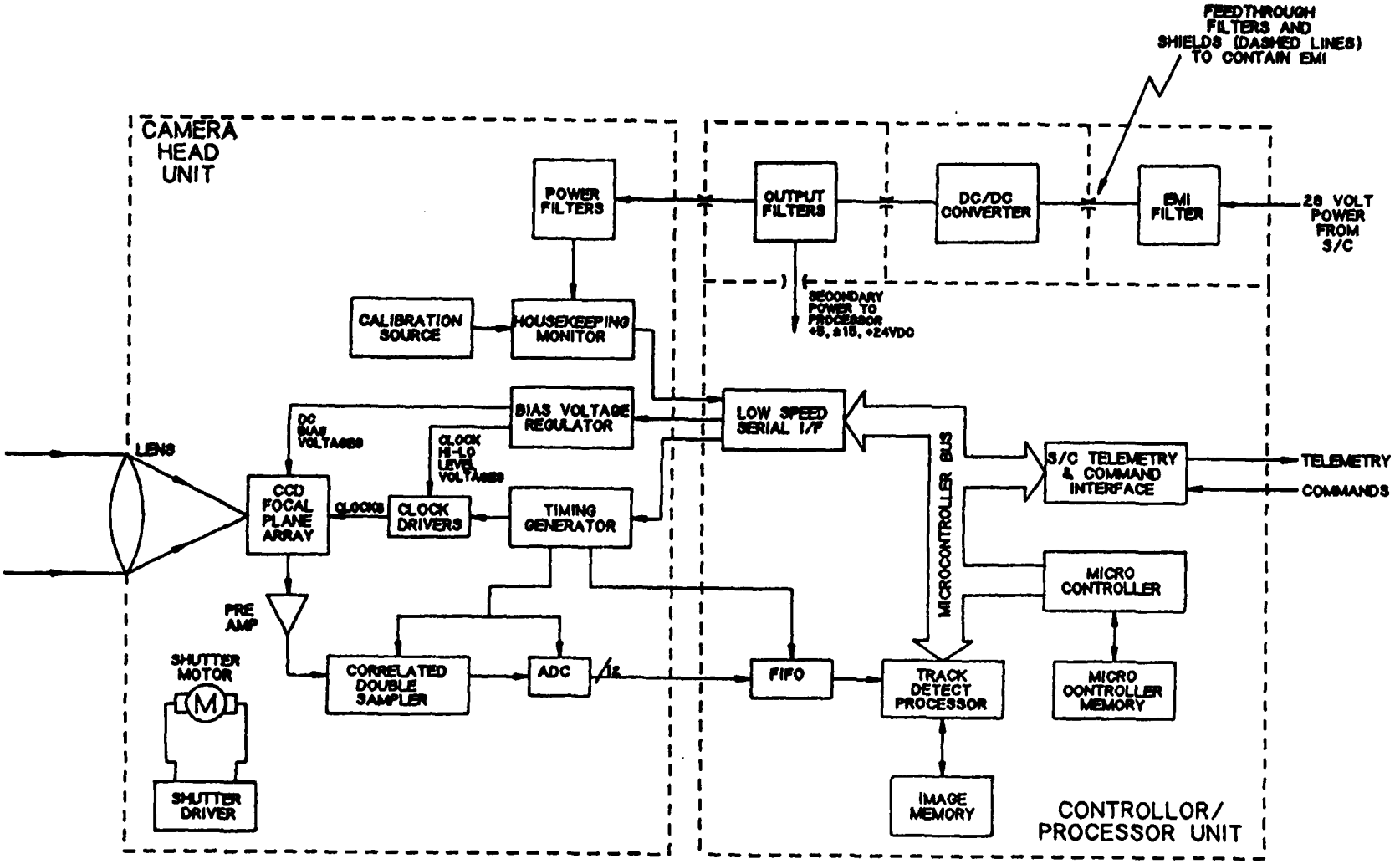

Figure 5

Block diagram of the SPI Camera and Signal Processor

REPORT DOCUMENTATION PAGE

Form Approved
OMB No. 0704-0188

1. AGENCY USE ONLY (*Leave blank*)	2. REPORT DATE	3. REPORT TYPE AND DATES COVERED
	7 April 1994	Project Report

4. TITLE AND SUBTITLE

Proceedings of the 1994 Space Surveillance Workshop

5. FUNDING NUMBERS

C — F19628-90-C-0002

6. AUTHOR(S)

K.P. Schwan (Editor)

7. PERFORMING ORGANIZATION NAME(S) AND ADDRESS(ES)

Lincoln Laboratory, MIT
P.O. Box 73
Lexington, MA 02173-9108

8. PERFORMING ORGANIZATION REPORT NUMBER

STK-221 Volume II

9. SPONSORING/MONITORING AGENCY NAME(S) AND ADDRESS(ES)

ESC
Hanscom Air Force Base
Bedford, MA 01730

10. SPONSORING/MONITORING AGENCY REPORT NUMBER

ESC-TR-94-091

11. SUPPLEMENTARY NOTES

None

12a. DISTRIBUTION/AVAILABILITY STATEMENT

Approved for public release; distribution is unlimited.

12b. DISTRIBUTION CODE

13. ABSTRACT (*Maximum 200 words*)

The twelfth Annual Space Surveillance Workshop hosted by MIT Lincoln Laboratory was held 5–7 April 1994. The purpose of this series of workshops is to provide a forum for the presentation and discussion of space surveillance issues.

This *Proceedings* documents most of the presentations from this workshop that did not appear in Vol. I. The papers contained were reproduced directly from copies supplied by their authors (with minor mechanical changes where necessary). It is hoped that this publication will enhance the utility of the workshop.

14. SUBJECT TERMS	15. NUMBER OF PAGES 76
	16. PRICE CODE

17. SECURITY CLASSIFICATION OF REPORT	18. SECURITY CLASSIFICATION OF THIS PAGE	19. SECURITY CLASSIFICATION OF ABSTRACT	20. LIMITATION OF ABSTRACT
Unclassified	Unclassified	Unclassified	Same as report